applied sciences

MDPI

Article

Towards Improved Efficiency of Low-Grade Solar Thermal Cooling: An RSM-Based Multi-Objective Optimization Study

Abdelmajid Saoud [1,*] and Joan Carles Bruno [2]

[1] University of Gabes, National School of Engineers of Gabes, Laboratory of Applied Thermodynamic LR18ES33, Gabes 6029, Tunisia
[2] Universitat Rovira I Virgili, Mechanical Engineering Department, CREVER—Group of Applied Thermal Engineering, Av. Països Catalans 26, 43007 Tarragona, Spain; juancarlos.bruno@urv.cat
* Correspondence: abdelmajid.saoud@enig.u-gabes.tn

Featured Application

The proposed low-grade solar thermal absorption chiller provides a sustainable cooling solution for residential and commercial buildings in sun-rich regions. By operating efficiently at low driving temperatures achievable with evacuated flat plate collectors, the system reduces electricity consumption from conventional vapor compression systems and lowers greenhouse gas emissions. Its optimized design offers a cost-effective pathway for integrating renewable energy into HVAC applications, particularly in hot climates where cooling demand coincides with peak solar availability.

Abstract

This study investigates an integrated solar-driven single-effect H_2O–LiBr absorption chiller powered by low-grade thermal energy. A detailed thermodynamic model, comprising a solar collector, a thermal storage tank, and an absorption cycle, was developed using the Engineering Equation Solver (EES) software V10.561. A comprehensive parametric analysis and multi-objective optimization were then conducted to enhance both the energy and exergy performance of the system. The Response Surface Methodology (RSM), based on the Box–Behnken Design, was employed to develop regression models validated through analysis of variance (ANOVA). The generator temperature (78–86 °C), evaporator temperature (2.5–6.5 °C), and absorber/condenser temperature (30–40 °C) were selected as key variables. According to the results, the single-objective analyses revealed maximum values of COP = 0.8065, cooling capacity = 20.72 kW, and exergy efficiency = 39.29%. Subsequently, the multi-objective RSM optimization produced a balanced global optimum with COP = 0.797, cooling capacity = 20.68 kW, and exergy efficiency = 36.93%, achieved under optimal operating conditions of 78 °C generator temperature, 6.5 °C evaporator temperature, and 30 °C absorber/condenser temperature. The obtained results confirm the significance of the proposed low-grade solar absorption chiller, demonstrating comparable or superior performance to recent studies (e.g., COP ≈ 0.75–0.80 and ≈35–37%). This agreement validates the RSM-based optimization approach and confirms the system's suitability for sustainable cooling applications in low-temperature solar environments.

Keywords: absorption cooling system; response surface methodology; Box–Behnken design; exergy analysis; low-temperature solar collectors; multi-objective optimization

Academic Editor: Paulo Santos

Received: 3 October 2025
Revised: 20 October 2025
Accepted: 26 October 2025
Published: 28 October 2025

Citation: Saoud, A.; Bruno, J.C. Towards Improved Efficiency of Low-Grade Solar Thermal Cooling: An RSM-Based Multi-Objective Optimization Study. *Appl. Sci.* **2025**, *15*, 11518. https://doi.org/10.3390/app152111518

1. Introduction

1.1. Background and Motivation

Broad adoption of renewable energy sources is essential for reducing fossil fuel dependence, lowering carbon emissions, and enhancing global energy security [1,2]. Among these sources, solar energy stands out as the most abundant, versatile, and accessible form of renewable energy, capable of meeting substantial energy demands across various applications [3,4]. Solar energy can be harnessed through photovoltaic systems to generate electricity or via solar thermal collectors to supply heat. Furthermore, solar radiation serves as a versatile alternative for modern energy systems, as it can be concentrated to generate electricity [5]. The building sector accounts for roughly one-third of global energy use and about 25% of CO_2 emissions [6]. This represents significant potential for energy-efficiency improvements. In particular, heating, ventilation, and air-conditioning (HVAC) systems account for 35–40% of a building's total energy consumption [7]. Consequently, integrating solar-powered cooling technologies into buildings represents a promising strategy to reduce operational energy consumption and associated environmental impacts.

1.2. Importance of Absorption Chillers and Current Challenges

In this context, solar-driven cooling technologies, particularly absorption refrigeration systems (ARSs), have emerged as sustainable alternatives to traditional electricity-based cooling systems. These systems effectively align peak cooling demand with periods of high solar irradiation, making them particularly suitable for regions with strong solar potential [8]. Single-effect absorption chillers (SE-AC) using the water–lithium bromide (H_2O–LiBr) pair represent a promising ARS technology capable of operating with low-temperature heat sources and natural refrigerants, achieving coefficients of performance (COP) around 0.7 [9]. However, the performance of such systems is highly sensitive to design parameters, operating conditions, the number of stages or effects, heat-source characteristics, condensation method, application, working mode, cycle configuration, and working-fluid pair, emphasizing the need for rigorous thermodynamic analysis and optimization.

1.3. Literature Gaps and Related Work

Optimization plays a crucial role in improving the efficiency, reliability, and sustainability of energy systems. In solar-thermal-driven cooling systems, where energy availability is inherently intermittent, system performance is highly sensitive to operating conditions. Optimization minimizes energy losses, improves efficiency, and identifies optimal designs that balance multiple objectives.

Various optimization strategies have been applied to absorption refrigeration systems, particularly in the context of solar integration. These include both deterministic and advanced metaheuristic algorithms such as Genetic Algorithms (GAs), Particle Swarm Optimization (PSO), and Artificial Neural Networks (ANNs) [10–12]. For instance, Yang et al. [13] designed an optimized cascade cooling system for a polysilicon plant using Aspen Plus and MATLAB with a GA, achieving annual savings of USD 931,025, recovering 3.139 kW of waste heat, generating 2.404 kW of cooling, and saving 7.8 million kWh of energy. Bellos et al. [14] applied the Conjugate Directions Method in EES to optimize a solar ejector refrigeration system, identifying optimal generator temperatures and suitable refrigerants. R141b was found to be the most effective, with the system achieving a maximum COP of 0.234 and optimal generator temperatures between 114 °C and 157 °C. Absorption cooling performance can be significantly improved through system configuration enhancements, driving temperature adjustments, or the integration of advanced components. Saoud et al. [15] investigated a novel Single Effect Double Lift Absorption Chiller (SE-DL AC). At 88.7 °C, the SE-DL AC delivered more than ten times the cooling

capacity of a conventional system, with a comparable COP and a substantially higher glide temperature (36 °C vs. 3.5 °C). Domínguez-Inzunza et al. [16] compared five ammonia–lithium nitrate absorption systems, highlighting trade-offs between system complexity, COP, and generator temperature. Single-effect systems are simpler and offer nearly twice the COP of half-effect systems, whereas triple-effect systems achieve the highest COP but are more complex and require higher generator temperatures.

In absorption refrigeration systems (ARSs), the thermophysical properties of the working-fluid pair (refrigerant–absorbent) are crucial. While the NH_3–H_2O pair is suitable for sub-zero temperature applications, the H_2O–LiBr pair is preferred for air-conditioning and moderate cooling loads [17]. Kaushik and Kumar [18] conducted a thermodynamic analysis of a two-stage ammonia vapor absorption refrigeration system using NH_3–H_2O and NH_3–$LiNO_3$ working pairs. Their study found that the NH_3–$LiNO_3$ pair achieved a lower minimum evaporator temperature and a higher COP compared to the conventional NH_3–H_2O system. Wang et al. [19] examined nine ammonia-based working pairs incorporating ionic liquids, identifying four feasible options. Among these, NH_3/[mmim][DMP] achieved the highest COP of 0.79, while NH_3/[emim][TfN] (0.74), NH_3/[emim][SCN] (0.73), and NH_3/[bmim][BF_4] (0.70) also outperformed the conventional NH_3/H_2O system.

Despite extensive research on absorption cooling systems, several gaps remain in existing literature. Many previous studies focused on systems requiring high driving temperatures (typically above 90–100 °C), which limits their compatibility with low-grade solar heat sources. Moreover, most optimization studies concentrated on single-objective performance improvements, such as maximizing COP, while neglecting exergy efficiency and the coupled thermo-exergetic interactions among system components. Other investigations relied on specific collector types (e.g., evacuated tube or concentrating collectors) that, although efficient, are costly and less suitable for large-scale building integration. In addition, a considerable proportion of studies employed purely deterministic modeling approaches without using statistical optimization tools capable of revealing the interactions among key operating parameters. The present study addresses these shortcomings by developing a comprehensive thermodynamic and exergy model of a low-temperature solar-powered H_2O–LiBr absorption chiller driven by evacuated flat-plate collectors. The system is designed to operate efficiently at driving temperatures below 90 °C, thereby enhancing cost-effectiveness and applicability in hot, sun-rich regions. Moreover, a multi-objective optimization approach based on Response Surface Methodology (RSM) is applied to simultaneously maximize COP, cooling capacity, and exergy efficiency. This provides a balanced and holistic performance improvement compared with previous single-objective or high-temperature studies. Optimization of energy systems is also essential for achieving cost savings, reducing environmental impacts, and improving energy security. Ultimately, such optimization supports the transition toward zero-emission energy systems, which are vital for meeting the 1.5 °C climate target [20,21].

1.4. Objective, Scope, and Contributions

The objective of this study is to develop a comprehensive thermodynamic model of a single-effect water–LiBr absorption chiller powered by low-temperature solar energy, using the Engineering Equation Solver (EES V10.651) package. The model is employed to perform both deterministic and statistical optimization through Response Surface Methodology (RSM) based on the Box–Behnken Design (BBD). A detailed parametric investigation is conducted by varying key operating factors, including generator, evaporator, absorber, and condenser temperatures. This dual approach enables a physical understanding of performance trends while providing predictive regression models for optimal system operation.

The study also introduces several distinctive contributions to the field of solar- HVAC units. First, it demonstrates advanced RSM-based multi-objective optimization of a LiBr–H_2O single-effect chiller, offering a holistic and balanced approach to performance enhancement. Second, it addresses the underexplored integration of low-temperature solar collectors, specifically evacuated flat-plate collectors (EFPCs), which are cost-effective, widely available, and well-suited for large-scale applications in sun-rich regions. Finally, it bridges a critical research gap by coupling comprehensive thermodynamic modeling with rigorous statistical analysis. This combined framework captures both the physical and statistical sensitivities of operating parameters, yielding insights into system optimization that are not provided by earlier studies.

The application of RSM-based multi-objective optimization provides several advantages for the present study compared with traditional deterministic or single-variable optimization methods. It enables the simultaneous optimization of multiple performance indicators, namely COP, cooling capacity, and exergy efficiency, allowing for a balanced improvement of thermal and exergetic performance. In addition, RSM generates statistically validated regression models that capture the nonlinear interactions between decision parameters with high precision and consistency, ensuring robust predictive capability. The Box–Behnken Design further enhances computational efficiency by requiring a reduced number of simulations runs while maintaining statistical significance. Consequently, this hybrid thermodynamic–statistical framework increases model reliability, versatility, and reproducibility, making it well-suited for optimization of complex solar-assisted absorption systems.

2. System Description

The proposed solar cooling system comprises three modules designed to convert solar energy into cooling energy efficiently. Figure 1 represents the system diagram.

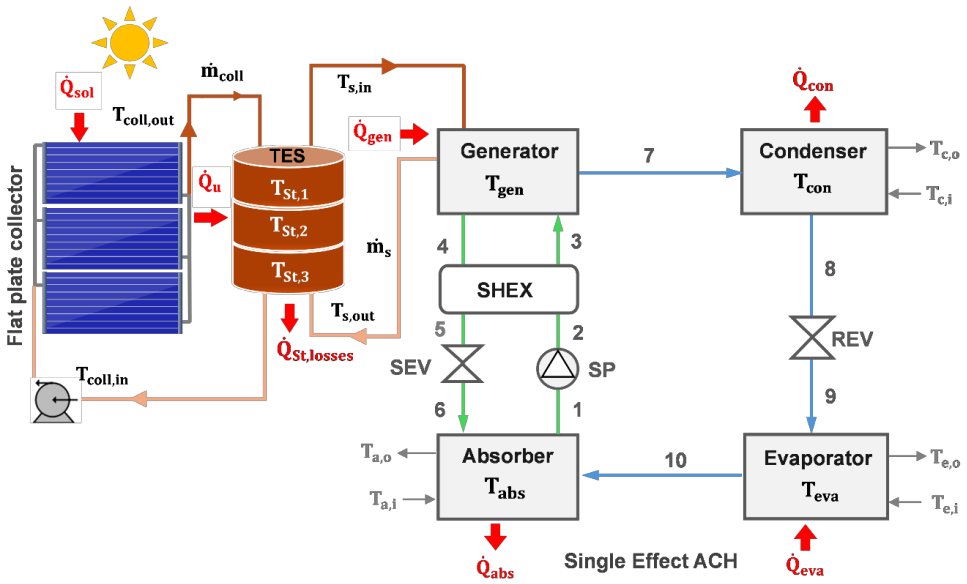

Figure 1. Schematic of the solar-driven cooling unit.

The solar energy collection system uses an array of evacuated flat-plate solar collectors to maximize cost-effectiveness. A well-insulated thermal storage tank stores the collected energy, ensuring a steady supply even though solar radiation is insufficient. Pressurized water is utilized as a medium for heat transfer in both the collecting field and the storage tank to avoid evaporation and preserve the liquid phase. The EFPC converts primary heat energy $\dot{Q}_{sol}$ into useful thermal energy ($\dot{Q}_u$). The upper section receives hot water

at $T_{coll,\ out}$, while the lower section receives cooler water at $T_{coll,\ in}$, which returns to the collector field. From the opposite side of the tank, hot water at $T_{s,in}$, flows into the heat recovery system, where it transfers heat to the chiller generator. The cooled HTF returns to the tank's lower section, completing the thermal circuit. The absorption chiller (AC) is a single-effect device that operates at low temperature. The cycle uses lithium bromide-water (water–LiBr) as the working pair, and water/steam as the refrigerant. It consists of two pressure levels (Low and high) and four main components: a generator, an evaporator, a condenser, and an absorber. A solution heat exchanger (SHEX) improves the coefficient of performance (COP). The system also includes a solution pump (SP) and two expansion valves (SEV and REV). The absorption cycle includes four fundamental processes:

- Generation (GE)—Thermal energy ($\dot{Q}_{gen}$): The generator is powered by a heat source, such as solar energy or waste heat, which evaporates water from the LiBr solution (State 7). The produced high-pressure vapor is directed to the condenser, while the weak solution (State 4) is returned to the absorber.
- Condensation (CO)—Heat Rejection: occurs when high-pressure vapor (State 7) condenses into liquid (State 8) in a condenser, releasing heat ($\dot{Q}_{con}$) to the surroundings.
- Evaporation (EV)—Cooling Effect: The cooling effect occurs when the liquid refrigerant expands through a valve (State 9) and enters the evaporator, absorbing heat from the cooling load ($\dot{Q}_{eva}$).
- Absorption (AB)—Solution Regeneration: The LiBr solution (State 1) absorbs the low-pressure vapor (State 10) in the absorber, resulting in a strong solution (State 6) and heat release ($\dot{Q}_{abs}$) contributing to environmental sustainability. The strong solution (States 2–3) is fed back into the generator to complete the cycle.

3. Mathematical Modeling

This section discusses the mathematical model of the solar-powered absorption cooling system depicted in Figure 1, which was developed and solved using Engineering Equation Solver (EES v10.561) [22]. The main assumptions are presented first, followed by energy and exergy analyses to determine system feasibility. The input data are shown in Table 1.

Table 1. Input data for the solar-driven single-effect absorption chiller.

Parameters	Value
FPC collecting area, A_{coll}	21 m^2
MFR of the collector field, $\dot{m}_{coll}$	0.056 $kg{\cdot}s^{-1}$
Collector aperture area, A_{ap}	1.84 m^2
Tank thermal loss coefficient, U_{st}	0.5 $W\ m^2\ K^{-1}$
Tank volume, V_{st}	3.5 m^3
Sun temperature, T_{sun}	5770 K
Solar irradiation, G_{tot}	1000 W/m^2
Ambient temperature, T_{amb}	298 K
Generator temperature, T_{gen}	82 °C
Evaporator (cooling) temperature, T_{eva}	4.5 °C
Condenser/absorber temperature, T_{con} , T_{abs}	35 °C
Solution heat exchanger effectiveness, ε_{SHEX}	65%

To simplify the mathematical model, the analysis employs standard assumptions for solar absorption systems, consistent with prior studies [23,24].

- The system operates under steady-state conditions,
- Pressure drops and heat losses throughout all components are negligible,
- The refrigerant is saturated at the outlets of the condenser and evaporator,

- The absorber's weak solution and the generator's strong solution are both saturated and in thermal equilibrium at their respective temperatures,
- Chemical, kinetic, potential, and associated exergy factors are ignored due to their small significance.
- The reference specific enthalpy (h_0) and entropy (s_0) or exergy calculations are defined at 25 °C and 1 atm.

3.1. Energy Analysis

The thermodynamic cycle is simulated based on the first law of thermodynamics and mass conservation equations. They are as follows:

$$\sum \dot{m}_{in} = \sum \dot{m}_{out} \quad (1)$$

$$\sum \dot{m} x_{in} = \sum \dot{m} x_{out}, \quad (2)$$

where $\dot{m}$ is the mass flow rate of the stream (either refrigerant or solution), and x is the mass fraction of lithium bromide (LiBr) in the water–LiBr solution.

Neglecting kinetic and potential energy effects, the energy conservation equation is:

$$\dot{Q}_{in} - \dot{W}_{in} + \sum_{in} \dot{m}_{in} h_{in} = \dot{Q}_{out} - \dot{W}_{out} + \sum_{out} \dot{m}_{out} h_{out}, \quad (3)$$

In this expression, the heat transfer rate between the control volume and its surroundings is represented by ($\dot{Q}$), ($\dot{W}$) signifies the rate of work transfer, and h is the specific enthalpy (kJ/kg).

3.1.1. Solar Energy Collecting Model

The total incident solar power on the collector $\dot{Q}_{sol}$ is calculated as a function of the FPC collecting area (A_{coll}) and total solar radiation (G_{tot}) based on the following expression:

$$\dot{Q}_{sol} = G_{tot} \cdot A_{coll}, \quad (4)$$

Equation (5) expresses the useful heat gain ($\dot{Q}_u$) as an energy balance of the working fluid, considering absorbed solar radiation, thermal losses, and heat transferred to the fluid.

$$\dot{Q}_u = \dot{m}_{coll} \cdot C_p (T_{coll,out} - T_{coll,in}), \quad (5)$$

where $\dot{m}_{coll}$ is the mass flow rate in the collector field, C_p is the specific heat capacity of the heat transfer fluid, and the term $(T_{coll,out} - T_{coll,in})$ are the outlet and inlet temperatures of the collector.

The thermal efficiency of a solar collector ($\eta_{th,coll}$) is calculated as the ratio of useful heat gain ($\dot{Q}_u$) to incident solar energy.

$$\eta_{th,coll} = \frac{\dot{Q}_u}{G_{tot} A_{coll}}, \quad (6)$$

The thermal efficiency ($\eta_{th,coll}$) is calculated with the following polynomial equation [25].

$$\eta_{th,coll} = \eta_0 - a_1 \frac{(Tf,_{moy} - T_{amb})}{G_{tot}} - a_2 \frac{(Tf,_{moy} - T_{amb})^2}{G_{tot}}, \quad (7)$$

In the above equation, the optical efficiency η_0 is equal to 0.759. The heat transfer coefficients are $\mathbf{a}_1$ = 0.508 W · m^{-2} · K^{-1} and a_2 = 0.007 W · m^{-2} · K^{-1}, representing the

baseline and temperature-dependent losses, respectively. $T_{f,moy}$ denotes the mean fluid temperature, T_{amb} the ambient temperature, and G_{tot} the total solar irradiance.

3.1.2. Thermal Storage Tank Model

The storage tank is modeled using a three-zone mixing approach, in which each zone is assumed to have a uniform temperature [26,27]. The heat transfer dynamics are described by energy balance equations, which serve as the basis for designing and evaluating the performance of the TES system.

Equations (8)–(10) present the governing differential equations for the different zones of the tank under steady-state conditions.

$$\dot{m}_{coll} \cdot C_p \cdot (T_{coll,out} - T_{st,1}) + \dot{m}_{coll} \cdot C_p \cdot (T_{st,2} - T_{st,1}) - U_{st} \cdot A_{st,1} \cdot (T_{st,1} - T_{amb}) = 0, \quad (8)$$

$$\dot{m}_{coll} \cdot C_p \cdot (T_{st,1} - T_{st,2}) + \dot{m}_{coll} \cdot C_p \cdot (T_{st,3} - T_{st,2}) - U_{st} \cdot A_{st,2} \cdot (T_{st,2} - T_{amb}) = 0, \quad (9)$$

$$\dot{m}_{coll} \cdot C_p \cdot (T_{st,2} - T_{st,3}) + \dot{m}_{coll} \cdot C_p \cdot (T_{s,out} - T_{st,3}) - U_{st} \cdot A_{st,3} \cdot (T_{st,3} - T_{amb}) = 0, \quad (10)$$

The thermal losses ($\dot{Q}_{St,\ losses}$) of the storage tank are the summary of the thermal losses of all the zones, is given by Equation (11) [28]:

$$\dot{Q}_{st,losses} = U_{st}\ A_{st,1}\ (T_{st,1} - T_{am}) + U_{st}\ A_{st,2}\ (T_{st,2} - T_{am}) + U_{st}\ A_{st,3}\ (T_{st,3} - T_{am}), \quad (11)$$

The stored energy for each zone is defined as follows:

$$\dot{Q}_{\ stored} = \dot{Q}_{\ input} - \dot{Q}_{\ output} - \dot{Q}_{\ Losses}, \quad (12)$$

The following assumptions are made to simplify the storage tank modeling under steady-state conditions: $T_{s,in}$ is equal to $T_{st,1}$; $T_{coll,in}$ is equal to $T_{st,3}$; $\dot{m}_{coll}$ is equal to $\dot{m}_s$; the overall heat transfer coefficient (U_{st}) is set at 0.5 W m^2 K^{-1} for a well-insulated tank [29]; and the tank geometry is assumed to have equal length and diameter, which does not affect the simulation results [29].

The storage tank volume (V_{st}) is calculated using Equation (13):

$$V_{st} = \frac{A_{tot}}{30} = \frac{\pi \cdot D_{st}^2 \cdot L_{st}}{4}, \quad (13)$$

The outer surface areas of the storage tank zones are determined using Equations (14)–(16) [14]:

$$A_{st,1} = \left[\frac{\pi \cdot D_{st}^2}{4}\right] + \left[\frac{\pi \cdot D_{st} \cdot L_{st}}{3}\right], \quad (14)$$

$$A_{st,2} = \left[\frac{\pi \cdot D_{st} \cdot L_{st}}{3}\right], \quad (15)$$

$$A_{st,3} = \left[\frac{\pi \cdot D_{st}^2}{4}\right] + \left[\frac{\pi \cdot D_{st} \cdot L_{st}}{3}\right], \quad (16)$$

The water mass in each zone is calculated using the following equation [14]:

$$M_{st} = \frac{\rho_f \cdot V_{st}}{3}, \quad (17)$$

3.1.3. Absorption Cooling System Model

This section presents the fundamental governing equations used in the thermodynamic modeling of the absorption chiller [30,31]. The energy input to the cycle, supplied as heat to the generator ($\dot{Q}_{gen}$) is determined by the following energy balance equation:

$$\dot{Q}_{gen} = \dot{m}_{ref}\, h_7 + \dot{m}_{str} h_4 - \dot{m}_{ws} h_3, \quad (18)$$

The heat absorbed by the absorber ($\dot{Q}_{abs}$) is calculated based on an energy balance between the inlet and outlet streams of the working fluid, as expressed below:

$$\dot{Q}_{abs} = \dot{m}_{ref} h_{10} + \dot{m}_{str} h_6 - \dot{m}_{ws}\, h_1, \quad (19)$$

The following equation expresses the heat rejection rate from the condenser ($\dot{Q}_{con}$):

$$\dot{Q}_{con} = \dot{m}_{ref} h_7 - \dot{m}_{ref} h_8, \quad (20)$$

The cooling load produced by the evaporator ($\dot{Q}_{eva}$) is determined by Equation (21).

$$\dot{Q}_{eva} = \dot{Q}_{cool} = \dot{m}_{ref}\, h_{10} - \dot{m}_{ref}\, h_9, \quad (21)$$

Equations (22) and (23) describe the mass flow rate balances in the absorber and generator, respectively. Equation (22) represents the energy balance for the LiBr mass flow rate, while Equation (23) accounts for the overall mass flow rate of both water and LiBr.

$$\dot{m}_{ws} \cdot X_{ws} = \dot{m}_{str} \cdot X_{str}, \quad (22)$$

$$\dot{m}_{str} + \dot{m}_{ref} = \dot{m}_{ws}, \quad (23)$$

The mass flow rate (Equation (24)) and the LiBr concentration in the water–LiBr solution (Equation (25)) at different state points are expressed as follows:

$$\dot{m}_{ws} = \dot{m}_3 = \dot{m}_2 = \dot{m}_1\,;\ \dot{m}_{str} = \dot{m}_6 = \dot{m}_5 = \dot{m}_4 = \dot{m}_{10} = \dot{m}_9 = \dot{m}_8 = \dot{m}_7, \quad (24)$$

$$X_{ws} = X_3 = X_2 = X_1;\ X_{str} = X_6 = X_5 = X_4;\ X_{ref} = X_{10} = X_9 = X_8 = X_7 = 0, \quad (25)$$

The following Equation describes energy transmission in a solution heat exchanger, considering both the hot and cold sides of the SHEX.

$$\dot{m}_{ws}(h_3 - h_2) = \dot{m}_{str}(h_8 - h_9), \quad (26)$$

Equation (26) defines heat exchanger efficiency in terms of enthalpy.

$$\eta_{SHEX} = \frac{h_8 - h_9}{h_8 - h_2}, \quad (27)$$

As previously mentioned, the solution and refrigerant valves, along with the fluid pump, are assumed to operate isenthalpically, meaning no heat exchange or work occurs. This assumption is reflected in Equations (28)–(30), which compare the enthalpy before and after each device.

$$h_5 = h_6, \quad (28)$$

$$h_8 = h_9, \quad (29)$$

$$h_2 \approx h_1, \quad (30)$$

The thermodynamic properties of the water–LiBr working pair and refrigerant are determined using the correlations developed by Patek and Klomfar [32,33] which are implemented as internal functions within the EES software V10.651.

The solution circulation ratio (SCR) is defined as the ratio of the weak solution's mass-flow rate exiting the absorber to that of the refrigerant.

$$SCR = \frac{\dot{m}_{ws}}{\dot{m}_{ref}} = \frac{X_{str}}{X_{str} - X_{ws}}, \quad (31)$$

The following equation illustrates the relationship between the temperatures of the absorber, generator, evaporator, condenser, and solution heat exchangers, as well as the overall heat conductance (UA).

$$\dot{Q}_i = UA_i \cdot LMTD_i, \quad (32)$$

In Equation (32), UA_i represents the overall heat transfer coefficient-area product for the component, while LMTD denotes the log mean temperature difference for that component. $\dot{Q}_i$, denotes the energy exchanged within the component, calculated based on Equations (18)–(21).

Equation (33) defines the LMTD in terms of the inlet and outlet temperatures of both the hot and cold streams, as shown below:

$$LMTD_i = \frac{(T_{h,\,in} - T_{c,\,out}) - (T_{h,\,out} - T_{c,in})}{\ln\left[\frac{T_{h,\,in} - T_{c,\,out}}{T_{h,\,out} - T_{c,in}}\right]}, \quad (33)$$

At that stage of the chiller modelling, it is noteworthy mentioning that the crystallization of the LiBr solution represents a major operational constraint in absorption chillers, occurring when the solution becomes supersaturated at low temperatures or high concentrations. In this study, all simulated operating points were verified to remain below the crystallization boundary of the LiBr–water system. According to published solubility data, the critical crystallization concentration is approximately 64–65% at 30 °C. To ensure stable operation, the model maintains a safety margin of at least 3–5 °C above the crystallization temperature for each corresponding concentration.

3.2. Exergy Analysis

Exergy analysis, grounded in the second law of thermodynamics and entropy generation, is a powerful tool for identifying process inefficiencies by quantifying irreversibilities. It determines the maximum useful work that can be extracted from energy sources or material flows in relation to a reference environment. Unlike conventional energy analysis, which overlooks energy degradation, exergy analysis uncovers actual losses and evaluates the quality of energy and material streams. This enables more targeted optimization and performance improvement.

$$\sum_{in} \dot{E}x_{in} = \sum_{in} \dot{E}x_{out} + \dot{E}x_D \quad (34)$$

$$\sum_{in} \dot{m}_{in} ex_{in} + \dot{E}x_{\dot{Q}} = \sum_{out} \dot{m}_{out} ex_{out} + \dot{E}x_{\dot{W}} + \dot{E}x_D, \quad (35)$$

where $\dot{E}x$ is the exergy rate (kW), $\dot{E}x_D$ is the exergy destruction rate, $\dot{E}x_{\dot{Q}}$ is the exergy transfer associated with heat transfer, and $\dot{E}x_{\dot{W}}$ is the exergy transfer associated with work.

$$\dot{E}_{\dot{Q}} = \dot{Q}_i \left(1 - \frac{T_{amb}}{T_{in}}\right), \quad (36)$$

T_{in} is the temperature at the system boundary where heat transfer occurs.

$$\dot{E}_{\dot{W}} = \dot{W}, \tag{37}$$

This study includes only physical exergy, excluding magnetic, electrical, nuclear, and surface tension effects, as well as kinetic, potential, and chemical exergies (the latter being considered minimal) [34]. Consequently, chemical exergy is omitted from all flows and components in the analysis. The physical exergy is defined as follows:

$$\dot{E}_{Ph} = (h - h_0) - T_0(s - s_0), \tag{38}$$

where h and s represent specific enthalpy and specific entropy, respectively, and h_0 and s_0 denote the fluid's specific enthalpy and entropy at the environmental reference state. Due to the nature of exergy balances, dead-state values cancel out [27]. Consequently, the exergy destruction (irreversibility) in each component of the solar absorption chiller is expressed as follows:

$$\dot{E}_{dst,\,gen} = \dot{m}_3 ex_3 - \dot{m}_3 ex_4 - \dot{m}_7 ex_7 + \dot{m}_{gen}(ex_{11} - ex_{12}), \tag{39}$$

$$\dot{E}_{dst,\,gen} = \dot{m}_3 ex_3 - \dot{m}_3 ex_4 - \dot{m}_7 ex_7 + \dot{m}_{gen}(ex_{11} - ex_{12}), \tag{40}$$

$$\dot{E}_{dst,\,con} = \dot{m}_7 ex_7 - \dot{m}_8 ex_8 + \dot{m}_{cond}(ex_{16} - ex_{15}), \tag{41}$$

$$\dot{E}_{dst,\,eva} = \dot{m}_9 ex_9 - \dot{m}_{10} ex_{10} + \dot{m}_{eva}(ex_{17} - ex_{18}), \tag{42}$$

$$\dot{E}_{dst,SHEX} = \dot{m}_3(ex_2 - ex_3) + \dot{m}_4(ex_4 - ex_5), \tag{43}$$

$$\dot{E}_{dst,SP} = \dot{m}_1(ex_1 - ex_2) + \dot{W}_{SPP}, \tag{44}$$

$$\dot{E}_{dst,SEV} = \dot{m}_6(ex_5 - ex_6), \tag{45}$$

$$\dot{E}_{dst,REV} = \dot{m}_9(ex_8 - ex_9), \tag{46}$$

3.3. Key Performance Indicators

This section outlines the key performance indicators (KPIs) for evaluating the solar-powered cooling system. The coefficient of performance (COP) is the primary parameter, defined as the ratio of cooling capacity to heat input, excluding the work of the pump.

$$COP = \frac{\dot{Q}_{eva}}{\dot{Q}_{gen} + \dot{W}_{Sp}} \cong \frac{\dot{Q}_{eva}}{\dot{Q}_{gen}}, \tag{47}$$

Another important metric is the system COP, which considers solar energy input instead of the generator heat input, as defined in Equation (48).

$$COP_{sys} = \frac{\dot{Q}_{eva}}{\dot{Q}_{sol}}, \tag{48}$$

The useful exergy output of the solar collector is evaluated using Equation (49)

$$\dot{E}_{coll} = \dot{Q}_u - \dot{m}_{coll} \cdot C_p \cdot T_{amb} \cdot \ln\left[\frac{T_{coll,out}}{T_{coll,in}}\right], \tag{49}$$

As shown in Equation (50), the exergy efficiency of the EFPC is calculated as the ratio of useful exergy output to the total solar exergy input.

$$\eta_{ex,col} = \frac{\dot{E}_{coll}}{\dot{E}_{sol}}, \tag{50}$$

The exergy flow of the incident solar irradiation, $\dot{E}_{sol}$ is calculated using the Petela model, as expressed in Equation (51) [35].

$$\dot{E}_{sol} = G_{tot} \cdot A_{coll} \cdot \left[1 - \frac{4}{3}\left(\frac{T_{amb}}{T_{sun}}\right) + \frac{1}{3}\left(\frac{T_{amb}}{T_{sun}}\right)^4\right], \tag{51}$$

The useful exergy output of the absorption chiller ($\dot{E}_{eva}$) is determined from the evaporator cooling load ($\dot{Q}_{eva}$) and indicates the exergy associated with the system's cooling effect [29,36].

$$\dot{E}_{eva} = -\dot{Q}_{eva}\left(1 - \frac{T_{amb}}{T_{eva}}\right), \tag{52}$$

The exergy input to the generator, ($\dot{E}_{gen}$) accounts for the energy used to power the absorption chiller. It considers the quality of the thermal energy entering the system, typically provided by a solar FPC or another heat source [37].

$$\dot{E}_{gen} = \dot{Q}_{gen}\left(1 - \frac{T_{amb}}{T_{gen}}\right), \tag{53}$$

Equation (51) is used to calculate the maximum theoretical efficiency for converting solar energy into useful work, considering the radiation source temperature (T_{sun} = 5770 K [38]), ambient temperature (T_{amb}), and the total incident solar energy flow ($\dot{Q}_{sol}$).

The exergetic efficiency of the chiller (η_{ex}) is defined as the ratio of the exergy extracted in the evaporator ($\dot{E}_{eva}$) to the exergy supplied to the generator ($\dot{E}_{gen}$) [39].

$$\eta_{ex} = \frac{\dot{E}_{eva}}{\dot{E}_{gen}}, \tag{54}$$

The above equation can be reformulated as follows:

$$\eta_{ex} = COP \cdot \frac{-\left(1 - \frac{T_{amb}}{T_{eva}}\right)}{\left(1 - \frac{T_{amb}}{T_{gen}}\right)}, \tag{55}$$

Another important metric that characterizes the distribution of irreversibilities within the absorption system is the irreversibility ratio (IR) of each component. It is defined as the ratio of exergy destruction in a specific component to the total exergy destruction in the system. It is expressed as [40]:

$$IR_i = \frac{\dot{E}_{dst}}{\sum \dot{E}_{dst,\,tot}}, \tag{56}$$

Equation (57) expresses the overall exergy efficiency of the solar-driven cooling system [39].

$$\eta_{ex,\,sys} = \frac{-\dot{Q}_{eva}\left(1 - \frac{T_{amb}}{T_{eva}}\right)}{G_{tot} \cdot A_{coll} \cdot \left[1 - \frac{4}{3}\left(\frac{T_{amb}}{T_{sun}}\right) + \frac{1}{3}\left(\frac{T_{amb}}{T_{sun}}\right)^4\right]}, \tag{57}$$

4. Process Simulation and Multi-Objective Optimization Approach

In this study, a comprehensive thermodynamic model is developed for the integrated system, which includes a solar collector, a thermal energy storage tank, and a water–LiBr absorption chiller, to evaluate both energy and exergy fluxes throughout the cycle.

4.1. Followed Methodology

Figure 2 illustrates the flowchart of the solving process implemented in the EES V10.651 software package, along with the steps followed in Design-Expert to optimize the chiller performance.

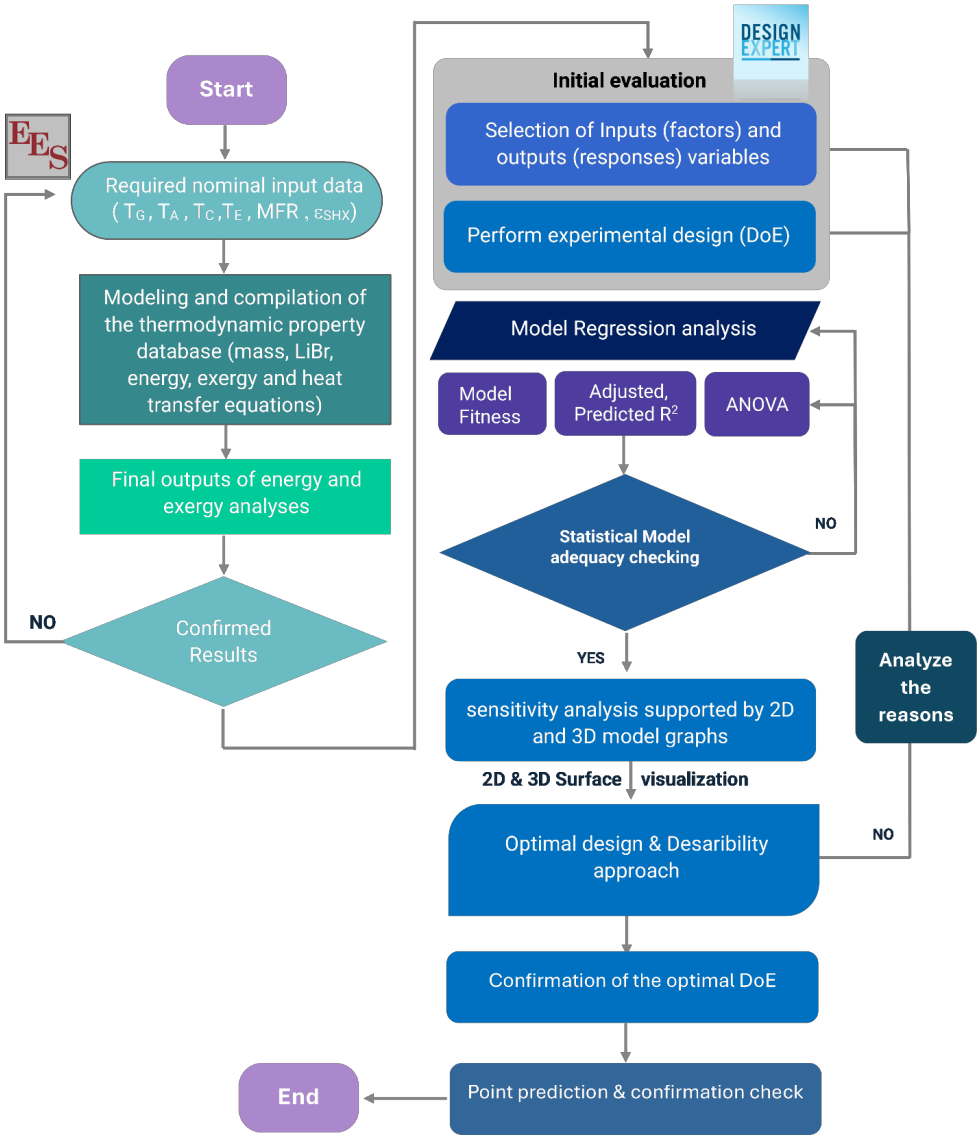

Figure 2. Schematic of the followed methodology.

In the following section, Response Surface Methodology (RSM) was applied to perform multi-objective optimization. RSM, a widely used Design of Experiments (DOE) technique, is effective for simultaneously developing and optimizing multiple objectives while minimizing both experimental and computational efforts [41,42]. This approach provides versatility in identifying the relative influence and interaction of key thermal parameters, allowing consistent prediction of system responses across different operating conditions. Hence, the method not only reduces the computational burden but also increases confidence in the statistical and physical consistency of the developed regression models.

All statistical analyses were performed using Design-Expert version 13:13.0.5.0 (Stat-Ease) [43]. RSM-based experiments are typically designed and implemented in four stages: (a) preparation, which defines the objectives, factors, and responses; (b) screening (process characterization), which identifies the most influential variables; (c) optimization, which aims to determine the optimal combination of factors to maximize or minimize the desired responses; and (d) verification, which validates the predicted results through confirming experiments.

4.2. RSM-BBD Optimization

The RSM study aimed to generate empirical models to predict and optimize three objective functions: COP (Equation (47)), cooling capacity (Equation (21)), and exergy efficiency (Equation (54)), using key chiller heat exchanger driving temperatures (T_{gen}; T_{eva}; T_{con}; T_{abs}). Table 2 summarizes the optimization variables and their associated ranges.

Table 2. DoE process variables with coded levels and ranges.

Factor	Name	Symbol (Units)	Min	Max	Coded Low	Coded High	Mean	Std. Dev.
A	Generator temperature	T_{gen}	78.00	86.00	$-1 \leftrightarrow 78.00$	$+1 \leftrightarrow 86.00$	82.00	2.62
B	Evaporator temperature	T_{eva}	2.50	6.50	$-1 \leftrightarrow 2.50$	$+1 \leftrightarrow 6.50$	4.50	1.31
C	Absorber temperature	T_{abs}	30.00	40.00	$-1 \leftrightarrow 30.00$	$+1 \leftrightarrow 40.00$	35.00	3.27
D	Condenser temperature	T_{con}	30.00	40.00	$-1 \leftrightarrow 30.00$	$+1 \leftrightarrow 40.00$	35.00	3.27

These optimizations aimed to enhance system performance by maximizing the coefficient of performance (COP), cooling capacity, and exergy efficiency. The Box–Behnken Design (BBD) was used for the experimental runs, which included 29 sets of experiments. The primary objective was to maximize the response variable by analyzing the interactions between the components and the response. BBD is ideal for a limited number of factors (typically three to five) and is favored for its simplicity and cost-effectiveness, as it requires fewer factor levels and avoids extreme values compared to the central composite design [44]. Quadratic equations were used to investigate the interactive effects of input parameters and responses. RSM, combined with ANOVA, was employed to create a regression model that links the decision parameters to the output responses. The following equation represents the general formulation of the RSM-built Box–Behnken Design (BBD) [45,46].

In this expression, the heat transfer rate between the control volume and its surroundings is represented by ($\dot{Q}$), while ($\dot{W}$) signifies the rate of work transfer.

$$Y_i = \beta_0 + \sum_{i=1}^{n} \beta_i X_i + \sum_{i=1}^{n} \beta_{ii} {X_i}^2 + \sum_{i=1}^{n-1} \sum_{j=i+1}^{n} \beta_{ij} X_i X_j + \in \quad (58)$$

where Y_i is the predicted response (e.g., COP, cooling capacity), β_0 is a constant coefficient, β_i, β_{ii} and β_{ij} are the linear, quadratic, and interaction coefficients, respectively, X_i and X_j are the independent variables, and $\in$ is the statistical error.

To facilitate the construction of the design matrix and eliminate the influence of different measurement units, the actual values of the independent variables (X_i) were

converted into dimensionless coded values (x_i) ranging from −1 (low), through 0 (center), to +1 (high). This transformation is performed using the following relationship:

$$x_i = \frac{X_i - X_0}{\Delta X} \quad (59)$$

where x_i is the coded value of the i_{ith} variable, X_i is its actual value, X_0 is the actual value at the center point, and ΔX is the step change value.

5. Model Validation

The accuracy of the model for the cooling cycle was validated by comparing the simulation results with recent literature, particularly the theoretical analysis of the water–LiBr system by Kaushik and Arora [47] and the experimental work of Florides et al. [48]. To ensure a fair comparison, identical input parameters were used throughout the validation process. Tables 3 and 4 present a comparative analysis between the theoretical predictions and experimental data, highlighting the differences between the literature results and those obtained from the current model. Based on this comparison, it is evident that both validation approaches exhibit a strong agreement between the theoretical predictions and the experimental observations, thereby confirming the reliability of the proposed model.

Table 3. Numerical verification of the ACH model.

Inputs Parameters		Output Parameters	Kaushik and Aurora [47]	Present Model	Absolute Deviation (%)
T_{gen} (°C)	87.8	$\dot{Q}_{gen}$ (kW)	3095.70	3084	0.378
T_{abs} (°C)	37.8	$\dot{Q}_{abs}$ (kW)	2945.27	2934	0.383
T_{con} (°C)	37.8	$\dot{Q}_{con}$ (kW)	2505.91	2507	0.043
T_{eva} (°C)	7.2	$\dot{Q}_{eva}$ (kW)	2355.45	2356	0.023
η_{SHEX} (%)	70	$\dot{Q}_{SHEX}$ (kW)	518.72	525.8	1.365
$\dot{m}_{ref}$ (kg·s^{-1})	1	COP	0.7609	0.764	0.407

Table 4. Experimental validation of the chiller model.

Inputs Parameters		Output Parameters	Florides et al. [48]	Present Model	Absolute Deviation (%)
T_{gen} (°C)	90.00	$\dot{Q}_{gen}$ (kW)	14.20	3084	0.378
T_{abs} (°C)	34.90	$\dot{Q}_{abs}$ (kW)	13.42	2934	0.383
T_{con} (°C)	44.30	$\dot{Q}_{con}$ (kW)	10.78	2507	0.043
T_{eva} (°C)	6.00	$\dot{Q}_{eva}$ (kW)	10.00	10.00	—
		$\dot{W}_{Sp}$ (kW)	0.29	0.29	—
$\dot{m}_{ref}$ (kg·s^{-1})	0.053	COP	0.704	0.764	0.407

6. Results and Discussion

This section presents the simulation results for the proposed system. The initial findings, under notional conditions, of the proposed unit (Figure 1) are summarized in Section 6.1. Sections 6.2–6.7 provide detailed analysis of the chiller's optimization. Finally, Section 8 focuses on comparing the results of the current study with existing literature.

6.1. Pre-Optimization Results

This section presents the primary results of the absorption chiller, illustrating the system's performance under default operating conditions. These findings serve as a baseline for comparison with the post-optimization outcomes.

The key indicators considered include the coefficient of performance (COP), cooling capacity ($\dot{Q}_{cool}$), and exergy efficiency (η_{ex}). The input parameters, such as the driving heat source temperature, mass flow rates, and operating temperatures of the main heat exchangers, are outlined in Table 1. The corresponding results are summarized in Table 5.

Table 5. Performance of the absorption chiller.

Components	Heat Transfer Rate (kW)	Heat Transfer Characteristics- Area Product (kW·C^{-1})
Generator	$\dot{Q}_{gen}$ = 14.60	UA_{gen} = 1.400
Condenser	$\dot{Q}_{eva}/\dot{Q}_{cool}$ = 11.09	UA_{eva} = 3.503
Evaporator	$\dot{Q}_{abs}$ = 14.03	UA_{abs} = 3.455
Absorber	$\dot{Q}_{con}$ = 11.66	UA_{con} = 2.364
Solution Heat Exchanger	$\dot{Q}_{SHEX}$ = 2.63	UA_{con} = -
Performance Indicators		
Coefficient of Performance (COP)		0.7596
System COP (COP_{sys})		0.528
Exergy efficiency of the chiller (η_{ex})		0.3495
Exergy efficiency of the solar cooling system ($\eta_{ex,\,sys}$)		0.042

Furthermore, the exergy analysis results are reported in this section. Figure 3 depicts the exergy destruction rates for the absorption of the chiller's components.

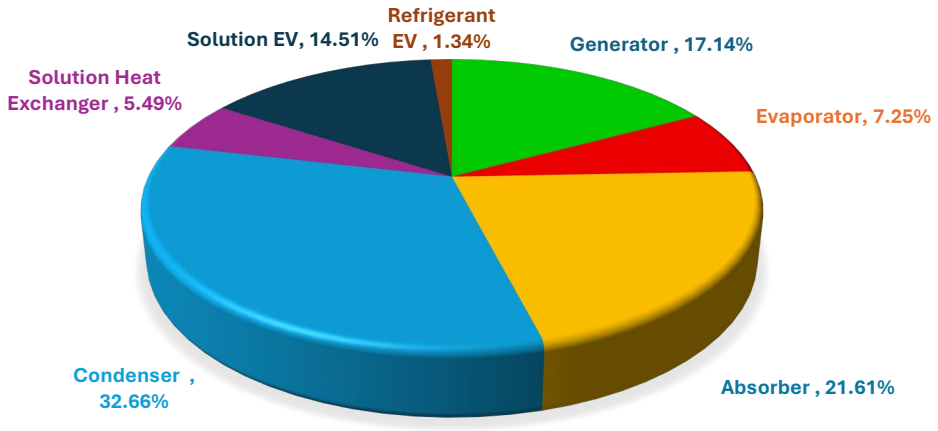

Figure 3. Exergy destruction rates distribution within the absorption chiller.

The condenser experiences the highest exergy destruction, accounting for 32.66% of the total exergy loss in the system. This result is expected, as the condenser typically operates with a significant temperature difference between the working fluid and the cooling medium, leading to increased irreversibilities and exergy losses. The absorber follows with the second-highest exergy destruction rate, contributing 21.61% of the total. This is due to the substantial temperature and concentration gradients inherent in the absorption process, which result in major thermodynamic irreversibilities.

Following the absorber, the generator accounts for 17.14 of the total exergy destruction, while the solution expansion valve contributes 14.51%. The evaporator and solution heat exchanger account for 7.25% and 5.49%, respectively. The refrigerant expansion valve and solution pump contribute the least to exergy destruction, at 1.34% and 0.00% (since the values are rounded to two decimal places), respectively. Figure 4 compares exergy losses and irreversibility ratios for the primary components of the single-effect water–LiBr absorption chiller.

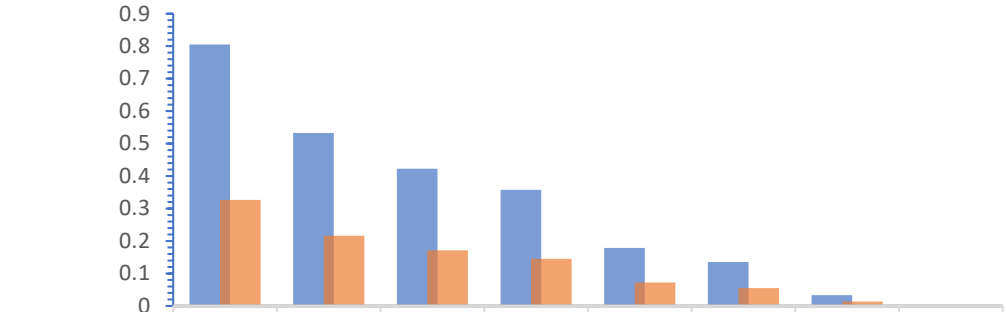

	Condenser	Absorber	Generator	Solution EV	Evaporator	Solution HX	Refrigerant EV	Solution pump
Exergy losses (kW)	0.8053	0.5327	0.4225	0.3576	0.1787	0.1353	0.0331	0.0001425
irreversibility ratio	0.3266	0.2161	0.1714	0.1451	0.0725	0.0549	0.01343	0.0000578

Figure 4. Exergy evaluation of the chiller.

The condenser experiences the highest exergy loss, estimated at 0.8053 kW, indicating significant inefficiencies in the heat rejection system. These losses may be attributed to factors such as high temperature variations, low thermal conductivity, fouling, or an insufficient heat exchange area. Other sources of exergy destruction include the absorber (0.5327 kW), generator (0.4225 kW), solution expansion valve (0.3576 kW), evaporator (0.1787 kW), solution heat exchanger (SHX) (0.1353 kW), refrigerant expansion valve (0.0331 kW), and the solution pump (1.425×10^{-4} kW).

6.2. RSM-Built Regression Model

The regression model accurately represents the relationship between the dependent and independent variables.

A 2^4 factorial design was constructed using Design-Expert Software (v13.0.5.0), with simulation data generated from the EES V10.561 program. The inlet temperatures of the generator, (T_{gen}), evaporator (T_{eva}), absorber (T_{abs}), and condenser (T_{con}) were selected as independent variables due to their direct influence on heat transfer, pressure levels, and thermodynamic performance. The main output responses were COP, cooling capacity ($\dot{Q}_{eva}/\dot{Q}_{cool}$) and the exergy efficiency (η_{ex}).

Table 6 presents the ranges of the independent variables and their corresponding responses within the experimental design framework. It includes the 29 randomized runs performed at different design points, representing the various combinations of input parameters.

Table 6. Design matrix: independent variables and system responses.

Run N°	T_{gen} (°C)	T_{eva} (°C)	T_{abs} (°C)	T_{con} (°C)	COP (-)	$\dot{Q}_{cool}$ (kW)	η_{ex} (%)
1	78	2.5	35	35	0.6934	5.472	37.5
2	86	4.5	35	40	0.7334	9.539	31.88
3	78	4.5	35	30	0.782	12.5	38.25
4	86	2.5	35	35	0.7479	11.55	35.94
5	78	4.5	35	40	0.5782	2.671	28.28
6	82	6.5	35	40	0.7416	8.844	30.57
7	82	2.5	35	40	0.625	3.872	31.79
8	82	2.5	40	35	0.6389	3.781	32.49
9	78	6.5	35	35	0.7711	10.43	33.8
10	86	4.5	35	30	0.7859	17.75	34.16
11	82	4.5	35	35	0.7597	11.03	34.95
12	78	4.5	30	35	0.7856	13.71	38.43
13	86	6.5	35	35	0.7846	16.25	30.56

Table 6. *Cont.*

Run N°	T_{gen} (°C)	T_{eva} (°C)	T_{abs} (°C)	T_{con} (°C)	COP (-)	$\dot{Q}_{cool}$ (kW)	η_{ex} (%)
14	82	6.5	30	35	0.8065	19.42	33.24
15	86	4.5	40	35	0.7329	8.912	31.86
16	82	4.5	40	30	0.7584	10.32	34.89
17	82	4.5	35	35	0.7597	11.03	34.95
18	82	2.5	35	30	0.7685	12.95	39.09
19	82	4.5	30	40	0.7632	12.14	35.11
20	86	4.5	30	35	0.7918	19.35	34.42
21	82	2.5	30	35	0.7725	14.06	39.29
22	82	4.5	30	30	0.8064	20.72	37.1
23	82	4.5	35	35	0.7597	11.03	34.95
24	82	6.5	35	30	0.8007	17.64	33
25	82	4.5	35	35	0.7597	11.03	34.95
26	82	6.5	40	35	0.742	8.204	30.58
27	82	4.5	35	35	0.7597	11.03	34.95
28	82	4.5	40	40	0.3936	1.058	18.11
29	78	4.5	40	35	0.6029	2.675	29.49

The regression equations derived for each response in coded form are as follows:

$$\mathbf{COP} = 0.7597 + 0.0303A + 0.0334B - 0.0714C - 0.0722D + 0.0378AD - 0.0804CD - 0.0308C^2 - 0.0380D^2 \quad (60)$$

$$\dot{\mathbf{Q}}_{\mathbf{cool}} = 11.03 + 2.99A + 2.43B - 5.37C - 4.48D - 0.0645AB + 0.1493AC + 0.4045AD - 0.2343BC + 0.0705BD - 0.1705CD - 0.1563A^2 + 0.0517B^2 + 0.2863C^2 - 0.2569D^2 \quad (61)$$

$$\boldsymbol{\eta}_{\mathbf{ex}} = 0.3495 - 0.0058A - 0.0203B - 0.0335C - 0.0340D + 0.0159AC + 0.0192AD - 0.0370CD - 0.0142C^2 - 0.0177D^2 \quad (62)$$

To improve model accuracy and achieve closer agreement between adjusted and predicted squared values, both cooling and exergy efficiency regression models were optimized using forward regression, excluding terms with *p*-values greater than 0.1.

6.3. ANOVA and Model Significance

Analysis of variance (ANOVA) was employed to evaluate the statistical significance of the developed models and the influence of operating parameters. The ANOVA results are summarized in Tables 7–9 for COP, cooling capacity, and exergy efficiency, respectively.

Table 7. ANOVA for the chiller COP.

Source	Sum of Squares	df	Mean Square	F-Value	*p*-Value	Remark
Model	0.1944	8	0.0243	21.21	<0.0001	**Significant**
$A - T_{gen}$	0.0110	1	0.0110	9.60	0.0057	
$B - T_{eva}$	0.0134	1	0.0134	11.66	0.0028	
$C - T_{abs}$	0.0612	1	0.0612	53.46	<0.0001	
$D - T_{con}$	0.0626	1	0.0626	54.66	<0.0001	
AD	0.0057	1	0.0057	5.00	0.0370	
CD	0.0259	1	0.0259	22.57	0.0001	
C^2	0.0066	1	0.0066	5.72	0.0267	
D^2	0.0100	1	0.0100	8.71	0.0079	
Residual	0.0229	20	0.0011			
Lack of Fit	0.0229	16	0.0014			
Pure Error	0.0000	4	0.0000			
Cor Total	0.2173	28				

Table 8. ANOVA for the cooling generation capability.

Source	Sum of Squares	df	Mean Square	F-Value	*p*-Value	Remark
Model	767.41	14	54.82	44,636.19	<0.0001	**Significant**
$A - T_{gen}$	107.36	1	107.36	87,422.89	<0.0001	
$B - T_{eva}$	70.58	1	70.58	57,475.29	<0.0001	
$C - T_{abs}$	346.15	1	346.15	2.819×10^5	<0.0001	
$D - T_{con}$	240.81	1	240.81	1.961×10^5	<0.0001	
AB	0.0166	1	0.0166	13.55	0.0025	
AC	0.0891	1	0.0891	72.56	<0.0001	
AD	0.6545	1	0.6545	532.95	<0.0001	
BC	0.2195	1	0.2195	178.73	<0.0001	
BD	0.0199	1	0.0199	16.19	0.0013	
CD	0.1163	1	0.1163	94.69	<0.0001	
A^2	0.1584	1	0.1584	129.02	<0.0001	
B^2	0.0173	1	0.0173	14.12	0.0021	
C^2	0.5318	1	0.5318	433.05	<0.0001	
D^2	0.4281	1	0.4281	348.64	<0.0001	
Residual	0.0172	14	0.0012			
Lack of Fit	0.0172	10	0.0017			
Pure Error	0.0000	4	0.0000			
Cor Total	767.43	28				

Table 9. ANOVA results for the exergy efficiency.

Source	Sum of Squares	df	Mean Square	F-Value	*p*-Value	Remark
Model	0.0437	9	0.0049	22.49	<0.0001	**Significant**
$A - T_{gen}$	0.0004	1	0.0004	1.85	0.1894	
$B - T_{eva}$	0.0049	1	0.0049	22.88	0.0001	
$C - T_{abs}$	0.0134	1	0.0134	62.26	<0.0001	
$D - T_{con}$	0.0138	1	0.0138	64.07	<0.0001	
AC	0.0010	1	0.0010	4.71	0.0428	
AD	0.0015	1	0.0015	6.84	0.0170	
CD	0.0055	1	0.0055	25.32	<0.0001	
C^2	0.0014	1	0.0014	6.42	0.0203	
D^2	0.0021	1	0.0021	9.95	0.0052	
Residual	0.0041	19	0.0002			
Lack of Fit	0.0041	15	0.0003			
Pure Error	0.0000	4	0.0000			
Cor Total	0.0478	28				

In statistics, a highly significant model is indicated by a lower probability value (p-value < 0.05) [49] and a greater Fisher test (F-test) value [50], suggesting a 95% confidence level [51].

The F-value is a statistic calculated as the ratio of a source's mean square to the residual mean square, testing whether the variation explained by the model is significant relative to unexplained variation. The associated p-value (Prob > F) quantifies the probability of observing an F-value at least as extreme as the one calculated, assuming the null hypothesis that there are no true factor effects, is correct. The p-values for all models are less than 0.0001, indicating strong statistical significance at the 95% confidence level. The corresponding F-values (21.21 for COP, 44,636.19 for $\dot{Q}_{cool}$ and 22.49 for η_{ex}) further demonstrate their robustness and reliability. The F- and p-values for the COP response (Table 7) show that the linear terms are statistically significant ($p < 0.05$). Only AD and CD are substantial among the interaction terms, while the quadratic terms A^2, B^2, and C^2 also contribute notably to the model. For the second response, the cooling capacity (Table 8), all terms, A, B, C, D, AB, AC, AD, BC, BD, CD, A^2, B^2, C^2, and D^2 are statistically significant ($p < 0.05$), confirming their contribution to the overall model significance. Regarding the final investigated response

(Table 9), all model terms are found to be statistically significant except for the generator temperature (A). Another approach to evaluating model reliability involves statistical indicators such as R^2, adjusted R^2, predicted R^2, and the coefficient of variation (CV), as shown in Table 10. An R^2 approaching 1.0, combined with a difference of less than 0.2 between the predicted and adjusted R^2, further validates their adequacy [52]. According to [50] models with R^2 values above 80% are generally deemed statistically significant.

Table 10. ANOVA-based fit metrics for system responses.

System Outputs	COP	$\dot{Q}_{cool}$	η_{ex}
R squared (R^2)	0.8946	1.0000	0.9142
Adjusted R^2(R^2_{adj})	0.8524	1.0000	0.8735
Predicted R^2(R^2_{prd})	0.6667	0.9999	0.7155
Difference ($R^2_{adj} - R^2_{prd}$)	0.1857	0.00001	0.158
Adequate Precision	19.4586	781.6910	20.5716
Coefficient of variation (%)	4.63	0.3186	4.37
Mean	0.7312	11	0.3361
Std. Dev.	0.0338	0.0350	0.0147

Table 10 shows that the models for all system outputs had high R^2 values (the proportion of total variation explained by the model), high Adjusted R^2 values (a version adjusted for the number of predictors to provide a more reliable quality indicator), and high predicted R^2 values (a measure of how well the model predicts new observations), confirming their strong predictive accuracy. The R^2 = 1.0000 results from the regression analysis based entirely on deterministic simulation data from the thermodynamic model. Because the input–output relationships are defined by exact equations without experimental uncertainty, the fitted RSM model reproduces these data points perfectly, yielding R^2 = 1.0000. This does not indicate overfitting but rather the numerical precision of the simulation. The differences between adjusted R^2 and predicted R^2 values (0.1857, 0.00001, and 0.158 for COP, $\dot{Q}_{cool}$ and η_{ex}, respectively) indicates good model consistency.

Furthermore, the adequate precision statistic measures the signal-to-noise ratio; a value greater than 4 is generally desirable as it indicates a sufficient signal for the model to be used to navigate the design space [50]. The adequate precision ratios (19.46, 781.69, and 20.57) exceed the minimum threshold of 4, validating the models' robustness in exploring the design space. In addition, the low coefficients of variation (4.63%, 0.32%, and 4.37%) confirm excellent reproducibility [53]. The Coefficient of variation (C.V) is the ratio of the standard error of the estimate to the mean value of the observed response, expressed as a percentage. A lower C.V. value (typically below 10%) indicates better reproducibility and reliability of the experiments [50]. Overall, these statistical indicators demonstrate that the developed quadratic models are reliable, statistically significant, and suitable for accurate performance prediction.

6.4. Statistical Model Assessment

Diagnostic plots from the ANOVA analysis were used to evaluate the relevance, performance, and predictive accuracy of the BBD-RSM models. The most informative plots are the predicted vs. actual and normal probability plots, presented for COP (Figure 5a,b), cooling capacity (Figure 5c,d), and exergy efficiency (Figure 5e,f).

The plots indicate that the developed models are adequate, with predicted values closely matching the actual measurements. Linear regression fits between predicted and actual values yielded R^2 values of 0.8946, 1.0000, and 0.9142, confirming the models' high significance and excellent predictive capability. Minor divergences in the plots reflect minimal inaccuracies, further validating the models' robustness. The normal probability

plots (Figure 5b,d,f) show data points roughly aligned along the diagonal, indicating normally distributed residuals and supporting the models' adequacy and reliability.

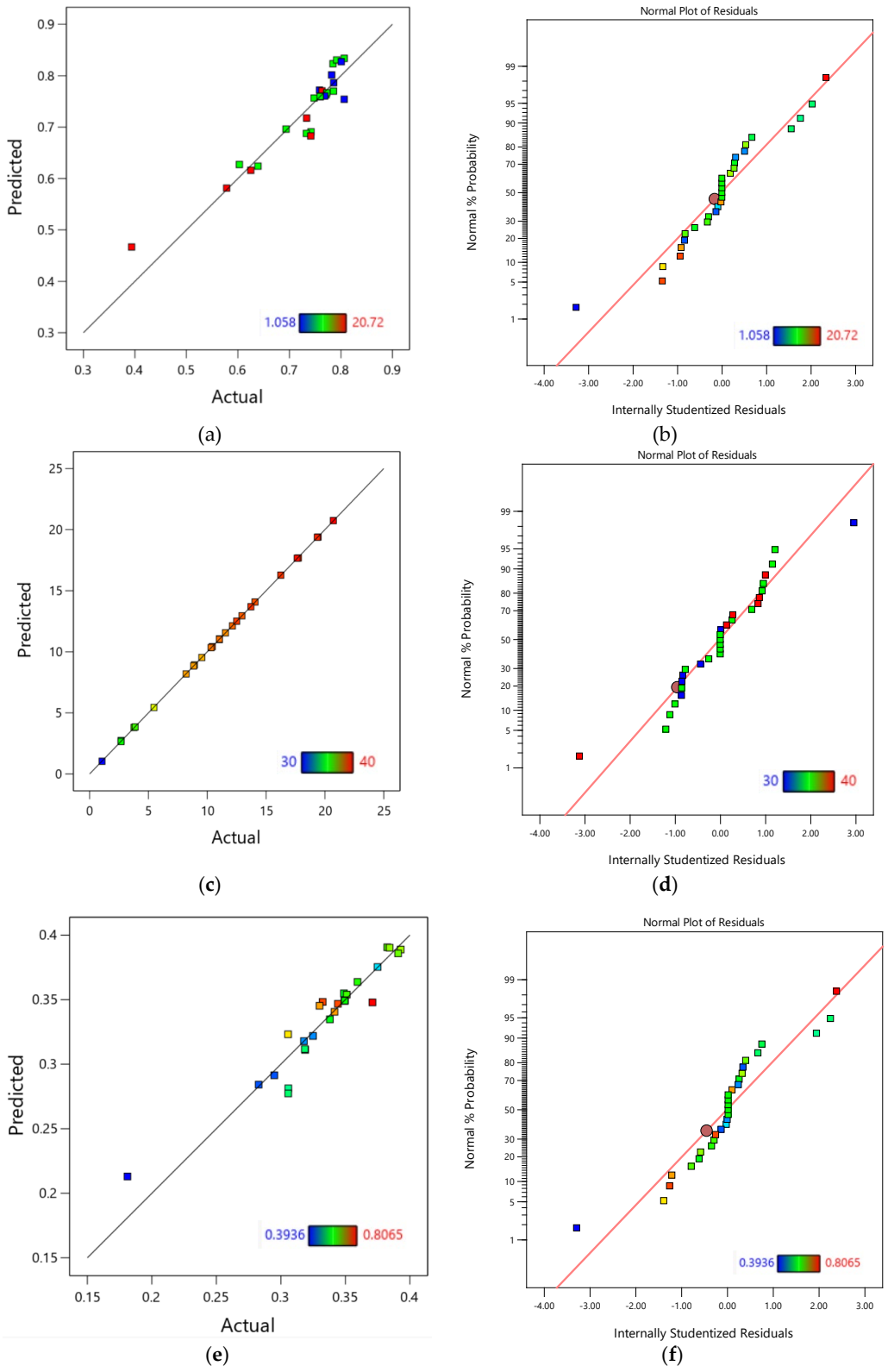

Figure 5. Diagnostic plots of the developed empirical model equations: (**a**) Predicted versus actual values for COP; (**b**) Normal probability plot of residuals for COP; (**c**) Predicted versus actual values for cooling capacity; (**d**) Normal probability plot of residuals for cooling capacity; (**e**) Predicted versus actual values for exergy efficiency; (**f**) Normal probability plot of residuals for exergy efficiency.

6.5. Parametric Analysis: Interaction Effects of Key Process Variables

In this section, the effects of the selected decision variables, the main heat exchanger temperatures, including those of the generator, evaporator, absorber, and condenser, on the COP, cooling capacity, and total exergy efficiency are investigated. To explore the interactions and mutual effects of these factors, two-dimensional (2D) contour plots and three-dimensional (3D) response surface plots are employed. These graphical tools illustrate the interaction between variable pairs while keeping the other parameters fixed at their center (nominal) values.

6.5.1. Assessment of the Effect of Decision Variables on the System COP

The COP model identified two significant two-way interactions: $T_{abs} - T_{con}$ (CD) and $T_{gen} - T_{con}$ (AD). These interactions were selected based on their strong model fit and statistical significance. The CD interaction showed a significant negative impact (F = 22.57, p = 0.0001), followed by the AD interaction (F = 5.00, p = 0.0370), highlighting the combined effect of heat input and rejection.

Figure 6a,b illustrates the interaction between the selected variables and the COP. As shown in the 2D contour plot (Figure 6a), the COP increases from approximately 0.5 in the top-right to about 0.8 in the bottom-left region, indicating that both T_{gen} and T_{con} have a detrimental impact on performance. Increasing either temperature results in a monotonic decrease in COP, suggesting that lower values improve efficiency. This tendency is supported by the 3D surface plot Figure 6b, which slopes downward from the front-left (low T_{gen} and T_{con}) to the back-right (high T_{gen} and T_{con}), indicating that optimal performance occurs at minimal levels of both inputs. The absence of sharp curvature or inflection indicates that the interaction between T_{gen} and T_{con} is relatively linear and smooth. As shown in Figure 6a–d, when T_{gen} increases, the heat input to the generator rises more rapidly than the cooling capacity, leading to a slight decrease in COP. This trend reflects the intrinsic thermodynamic behavior of the single-effect LiBr–H_2O cycle when analyzed in isolation, with other operating temperatures kept constant. Physically, an increase in both T_{gen} and T_{con} disrupts the thermodynamic balance of the cycle, amplifying exergy destruction in key components and significantly reducing overall system performance.

The 2D contour plot (Figure 6c) and 3D surface plot (Figure 6d) illustrates the variation of the COP as a function of generator and condenser temperatures ($T_{gen} - T_{con}$). The response surface shows that the COP reaches its highest value of around 0.80 in the region with the most favorable thermodynamic conditions for system operation, such as high generator temperatures and low condenser temperatures (bottom-left zone). Physically, increasing the generator temperature enhances refrigerant desorption, while decreasing the condenser temperature improves condensation, both of which contribute to a higher COP. Moving away from these optimal conditions leads to reduced thermal efficiency and increased irreversibility, as indicated by the decreasing COP in the response surface plots. Thus, precise control of both parameters is crucial for maximizing system performance.

The interaction between the remaining factors has been simplified because they have no substantial effect on the system's response (Equation (60)). The results in Table 6 indicate that the single-objective optimization for maximizing the system's Coefficient of Performance (COP) is achieved under specific conditions:

- A: Generator temperature (T_{gen}) = 82 °C;
- B: Evaporator temperature (T_{eva}) = 6.5 °C;
- C: Absorber temperature (T_{abs}) = 30 °C;
- D: Condenser temperature (T_{con}) = 35 °C.

Under these conditions, the system reaches its maximum COP of 0.8065.

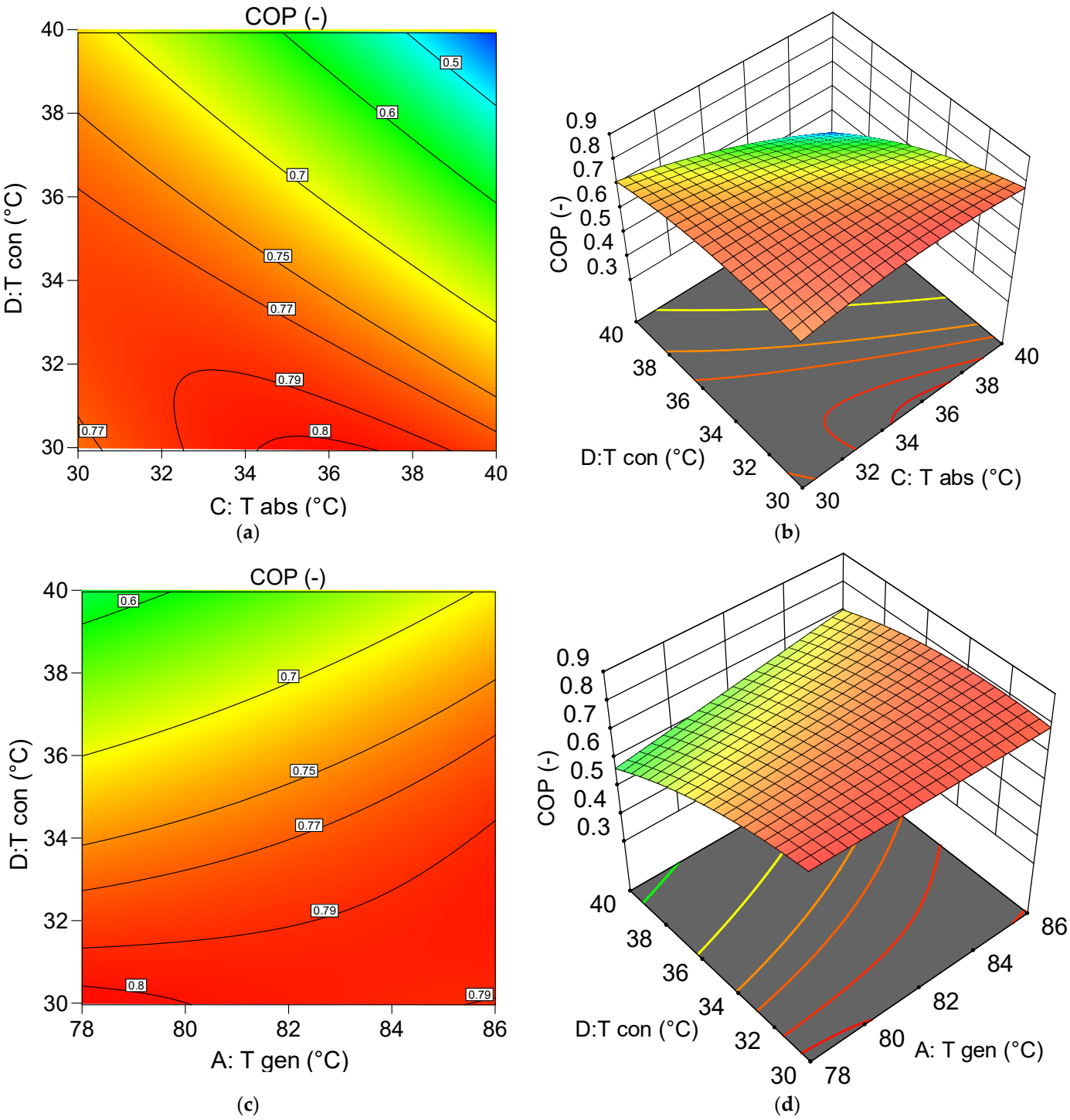

Figure 6. Interaction effects of decision variables on the chiller COP: (**a**) 2D contours of (T_{abs} − T_{con}); (**b**) 3D contours of (T_{abs} − T_{con}); (**c**) 2D contours of (T_{gen} − T_{con}) 2D contours; (**d**) 3D contours of (T_{gen} − T_{con}).

6.5.2. Assessment of the Effect of Decision Variables on the System Chiller Generation Capability

The interactions between the generator and condenser (AD) and the evaporator and absorber (BC) significantly impact cooling capacity, with F-values of 532.95 and 178.73, respectively ($p < 0.0001$). The contour and surface plots presented in Figure 7a,b illustrate the variation in cooling capacity as a function of the interaction AD (T_{gen} − T_{con}). The response surface shows a linear and steady increase in cooling output from approximately

5 to 17.5 kW, with the highest values occurring at higher generator temperatures and lower condenser temperatures. This pattern aligns with the thermodynamic principles of absorption cycles: raising the generator temperature enhances refrigerant vaporization, while lowering the condenser temperature facilitates more effective heat rejection, improving the driving potential and boosting the system's cooling capacity. The optimal region is in the bottom-right corner of the plot, where T_{gen} = 82.5–86 °C and T_{con} = 30–32 °C and where the cooling output reaches its maximum.

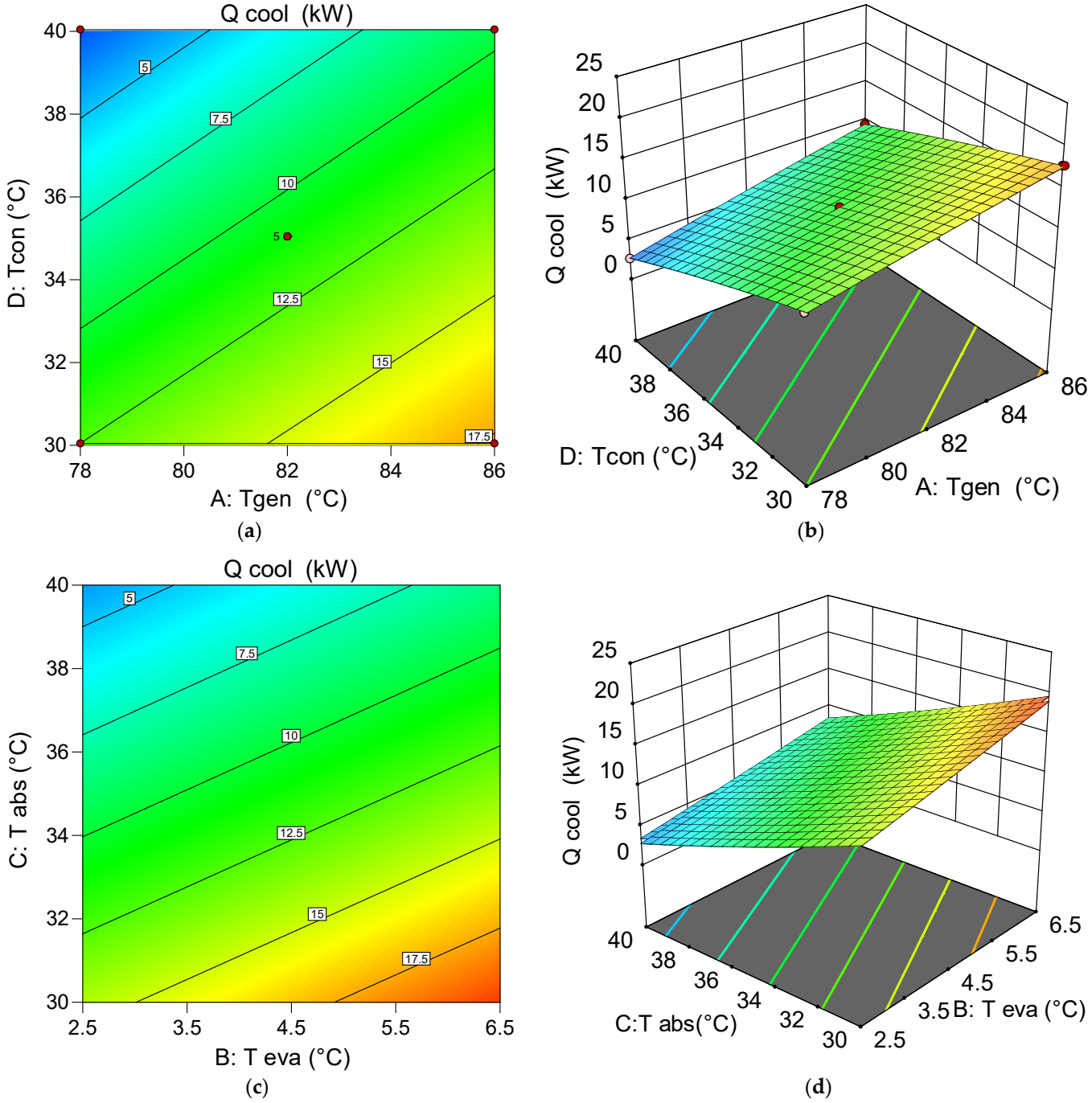

Figure 7. Interaction effects of decision variables on the chiller generation capability: (**a**) 2D contours of ($T_{gen} - T_{con}$); (**b**) 3D contours of ($T_{gen} - T_{con}$); (**c**) 2D contours of ($T_{eva} - T_{abs}$): (**d**) 3D contours of ($T_{eva} - T_{abs}$).

Figure 7c,d illustrates the interaction effect of the temperature difference between the evaporator and the absorber ($T_{eva} - T_{abs}$), evaluated at a generator temperature of

81.50 °C and an absorber temperature of 34.30 °C. The results show that the proposed system achieves its maximum cooling output, exceeding 18 kW, when the evaporator operates at its highest temperature and the absorber at its lowest. The system's cooling capacity improves under the following conditions: (a) when the evaporator temperature increases, allowing more heat to be absorbed as latent heat, and (b) when the absorber temperature decreases, enhancing the efficiency of the absorption process. Together, these conditions optimize the refrigerant cycle, increasing mass and heat transfer rates, and maximizing cooling output, as shown in the plots. ANOVA results (Table 8) indicate statistical significance for all main effects, two-way interactions (AB, AC, BD, and CD), and quadratic terms (A^2, B^2, C^2, and D^2). The cooling output is particularly sensitive to the absorber and condenser temperatures (T_{abs} and T_{con}), the AD interaction, and the quadratic components C^2 and D^2. The cooling capacity was optimized as a single objective, reaching its maximum value under the specified working conditions: T_{gen} = 82 °C, T_{eva} = 4.5 °C, T_{abs} = 30 °C, and T_{con} = 30 °C, yielding an output of 20.72 kW.

6.5.3. Interaction Results of Decision Parameters on the Exergy Efficiency of the System

The exergy efficiency model highlights two significant interaction terms: absorber–condenser (CD) and generator–condenser (AD). The CD interaction had the most substantial statistical impact (F = 25.32, $p < 0.0001$), suggesting that increasing both absorption and condensation temperatures simultaneously elevates system irreversibility. The AD interaction (F = 6.84, $p = 0.0170$) revealed a moderate effect, suggesting that heat exchange between the generator and condenser zones affects second-law performance. These parameters were considered to account for the interconnected thermodynamic effects in the chiller cycle.

Figure 8a,b demonstrates the combined effect of T_{abs} and T_{con} on the exergy efficiency of the cooling system's exergy efficiency at temperatures of 79.28 °C and 4 °C for T_{gen} and T_{eva}. Both the 2D contour and 3D surface plots show a clear monotonic decrease in exergy efficiency as T_{abs} and T_{con} improve.

At lower temperatures, the exergy efficiency peaks at around 38% but decreases to approximately 25% as temperatures rise. This degradation is primarily due to a reduced absorption driving force and decreased mass transfer at higher T_{abs}, as well as poor heat rejection and increased condensation pressure at higher T_{con}. The combined effect of these factors increases entropy generation and absorber pressure, leading to synergistically negative thermodynamic losses. The consistently downward-sloping 3D surface, with no discernible local optima, reinforces the absence of non-linear benefits when adjusting the various temperatures independently. These findings are consistent with previous research, which has reported lower exergy and energy performances at high absorber and condenser temperatures. Figure 8c,d show the interaction effect of T_{gen} and T_{con} on the exergy efficiency of the chiller. As previously mentioned, exergy efficiency improves at lower condensing temperatures for lower generator temperatures. The optimal performance occurs within a generator temperature range of around 95 °C and a condenser temperature of 35 °C, where the system achieves a balance between driving force and thermal losses. The 2D contour plot illustrates that increasing the generator temperature beyond a certain point decreases exergy efficiency, indicating thermal inefficiencies and reduced performance at high input heat levels.

In contrast, higher condenser temperatures seem to increase cooling output, likely due to enhanced condensation and improved system stability. The system achieves optimal performance with a generator temperature range of 78 °C to 82.5 °C and a condenser temperature range of 30 °C to 35 °C, where a balance between driving force and thermal losses is reached. The 3D surface plot confirms this interaction by showing a decreasing surface

gradient from the optimal region toward higher generator temperatures (Figure 8d). The interactions among the other parameters have been simplified, with only the AC interaction considered, as indicated by the statistical results in Table 8 and Equation (62). According to the results presented in Table 6, the system's exergy efficiency was maximized through single-objective optimization, yielding the ideal combination of operating parameters:

- A: Generator temperature (T_{gen}) = 82 °C;
- B: Evaporator temperature (T_{eva}) = 2.5 °C;
- C: Absorber temperature (T_{abs}) = 30 °C;
- D: Condenser temperature (T_{con}) = 35 °C.

The optimized setup yields an exergy efficiency of 39.29%.

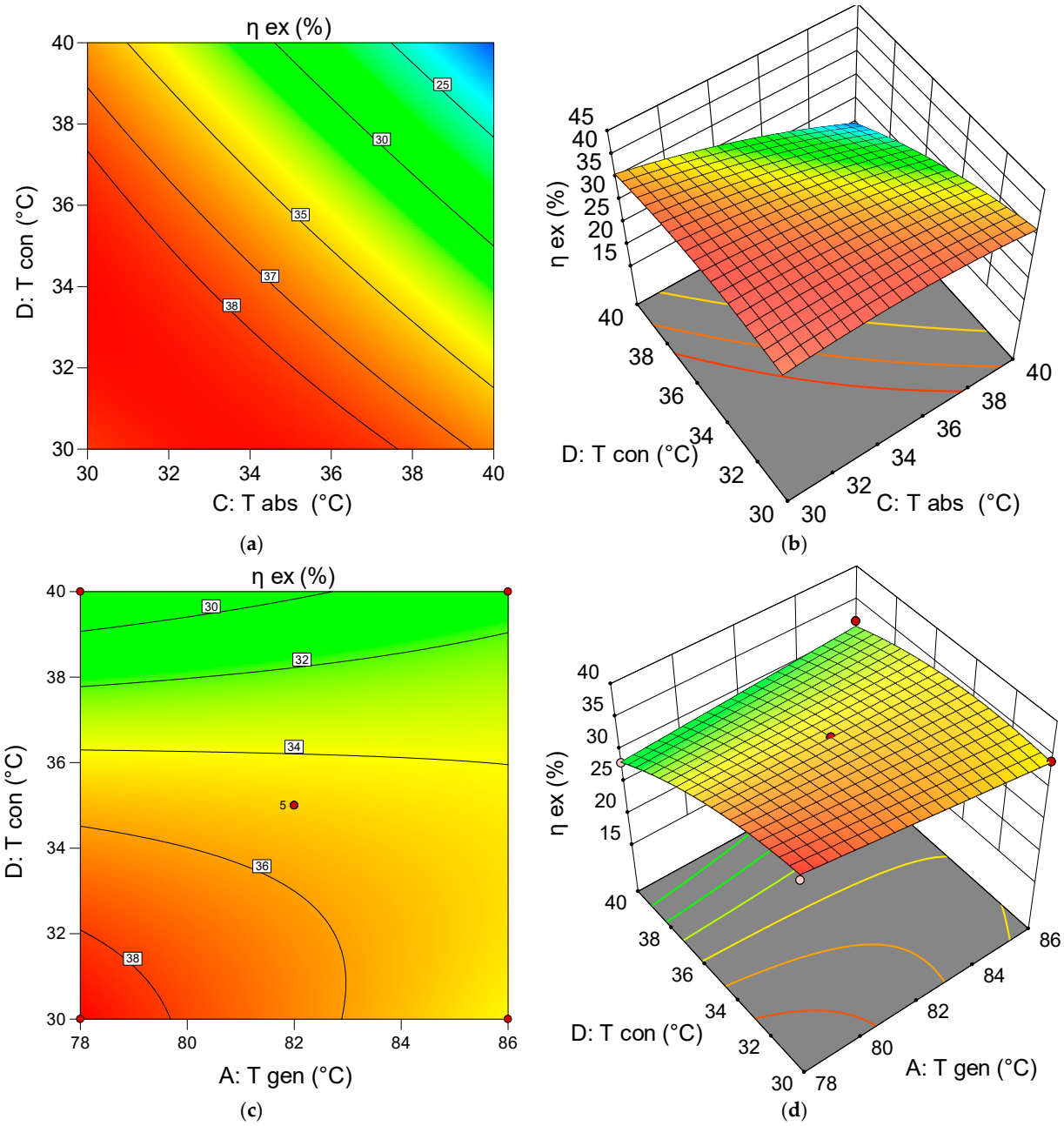

Figure 8. Interaction effects of decision variables on the exergy efficiency: (**a**) 2D contours of (T_{abs} − T_{con}); (**b**) 3D contours of (T_{abs} − T_{con}); (**c**) 2D contours of (T_{gen} − T_{con}) (**d**) 3D contours of (T_{gen} − T_{con}).

6.6. Desirability-Based Multi-Objective Optimization of System Output

The desirability function approach is used in Response Surface Methodology (RSM) for multi-objective optimization analysis. Each predicted response is converted into a dimensionless desirability value (d), which ranges from 0 (completely undesirable) to 1 (fully desirable) [54]. As the desirability value rises, the associated response improves [55]. This method simplifies multivariate optimization by reducing it to a single-objective problem. The primary goal is to identify operating conditions that simultaneously satisfy multiple response criteria while maximizing the overall desirability index. This section aims to identify operating conditions that achieve (a) maximum COP, (b) maximum cooling output, and (c) maximum exergy efficiency. To achieve this, the pairwise interactions of decision variables are systematically analyzed. It is important to note that all input variables have been set within their respective optimal ranges.

Figure 9 shows the desirability ramp graph, which represents the optimal input parameters and their corresponding output responses. Increasing generator and evaporator temperatures improves COP, $\dot{Q}_{cool}$, and η_{ex}. In contrast, lower absorber and condenser temperatures result in improved performance. Although the single-factor analysis indicated that COP tends to decrease with increasing T_{gen}, the multi-objective optimization simultaneously considers the combined effects of T_{gen}, T_{eva}, T_{abs}, and T_{con}. Within the studied range, the optimal trade-off occurs at a relatively higher generator temperature because the higher driving potential enhances the overall cooling capacity and exergy efficiency, thereby improving the global objective function. This does not contradict the individual trend but reflects the interactive influence of multiple parameters in the RSM model.

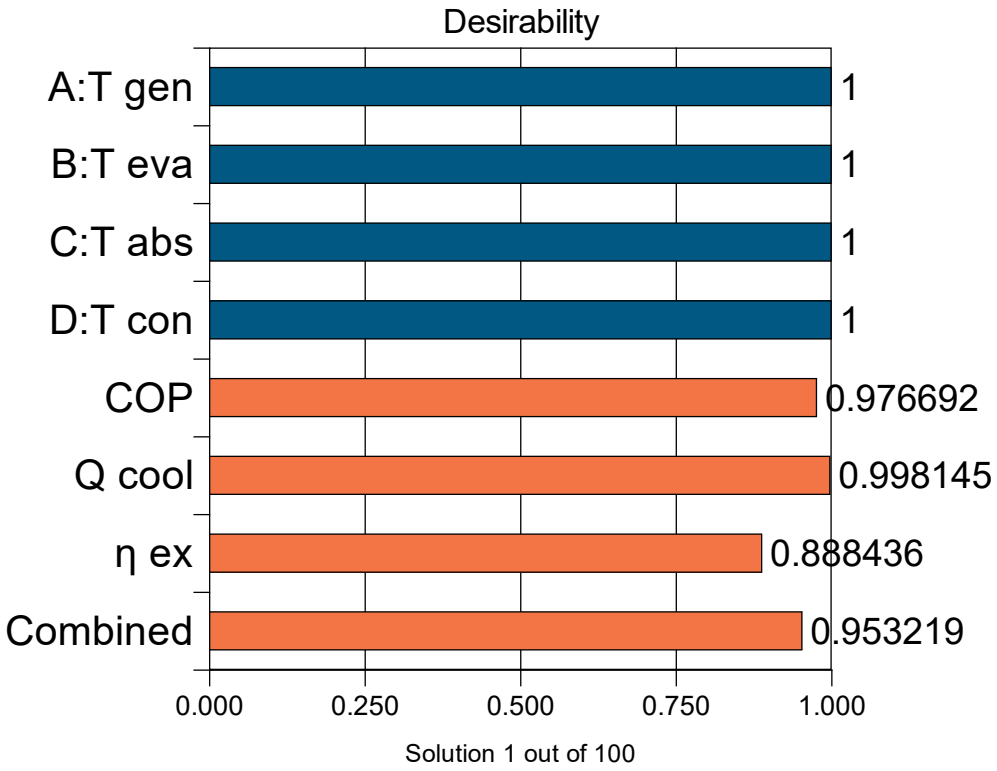

Figure 9. Desirability bar graph for the optimization case.

The optimal values for multi-objective optimization, a COP of 0.7969, a cooling capacity of 20.68 kW, and an exergy efficiency of 36.93%, are achieved at a generator temperature of 78 °C, an evaporator temperature of 6.5 °C, an absorber temperature of 30 °C, and a condenser temperature of 30 °C. The objective of the multi-objective optimization process is to identify a set of operating conditions that satisfactorily meet all performance criteria,

rather than merely achieving a desirability value of 1. Desirability functions serve as a mathematical tool to determine the most balanced and effective solution. Figure 9 displays the value of the combined desirability function, with an overall desirability score of 0.953 achieved for the optimized responses.

The goal of the optimization process is to identify a set of operating conditions that satisfy all performance requirements, rather than merely achieving a desirability value of one. Desirability functions are mathematical tools that help pinpoint the most balanced and effective solution. Figure 9 shows the combined desirability function, which resulted in an overall desirability score of 0.953 for the optimal responses.

6.7. Post Analysis

To evaluate the regression models for the single-effect water–LiBr absorption chiller, a confirmation test was conducted using Design-Expert's point prediction tool. The optimal conditions were applied as inputs, and the predicted values for COP, cooling capacity, and exergy efficiency were compared with the model's estimated outputs. As shown in Table 11, all predicted values fall well within the 95% confidence interval, validating the statistical reliability and accuracy of the RSM models. Since no experimental data were available, the simulated outputs from EES V10.651 closely matched the RSM predictions, and the minimal prediction error further confirms the consistency of both the simulation and optimization models.

Table 11. Confirmation test results.

Output Parameter	Predicted Value	Std. Error	95% CI Lower	95% CI Upper	Within CI?
COP	0.7971	0.0468	0.6995	0.8948	Yes
Cooling Capacity (kW)	20.6593	0.0617	20.5269	20.7916	Yes
Exergy Efficiency (%)	36.9371	2.1610	32.4140	41.4602	Yes

7. Literature-Based Performance Benchmarking

This study optimized a single-effect water–LiBr absorption chiller using key performance indicators: the coefficient of performance (COP), cooling capacity, and exergy efficiency. Under nominal operating conditions, the optimization resulted in significant performance improvements, including an 86.5% increase in cooling capacity, a 4.9% rise in COP, and a 5.7% improvement in exergy efficiency. These results validate the effectiveness of the RSM-based optimization approach in enhancing heat output and overall energy performance. To assess the robustness of the proposed optimization process, the present findings were compared with recent studies in the literature under similar operating conditions. Table 12 summarizes this comparison, highlighting that the optimized COP of 0.797 and exergy efficiency of 36.93% position the current system at the upper end of the performance range for single-effect water–LiBr absorption chillers. As shown, previous works such as those by Parham et al. [56], Al-Tahaineh [57], Kılıç and Kaynakli [36], and Kumar et al. [58] reported COP values between 0.75 and 0.95, while exergy efficiencies typically ranged from 25% to 36% depending on the operating temperatures and heat-source characteristics. Similarly, Shehadi [59], and Saoud et al. [31] achieved comparable COP values at moderate generator temperatures, though often with lower exergetic performance due to heat loss assumptions and non-optimized design parameters.

Recent investigations, including Zhao et al. [60] and Tawalbeh et al. [61], further confirm that COP values between 0.70 and 0.80 are typical for low-grade or geothermal-driven systems operating with generator temperatures below 90 °C. The present study's results are therefore consistent with, and in some cases superior to, these recent findings.

Moreover, by maintaining a moderate generator temperature of 78 °C, the system preserves high thermodynamic efficiency while remaining suitable for integration with low-grade or solar thermal energy sources. The combination of a balanced COP and high exergy efficiency demonstrates that the proposed RSM-based optimization provides an effective trade-off between energy performance and practical applicability.

Table 12. Comparison of the current optimization with literature studies.

Study	T_{gen} (°C)	T_{eva} (°C)	T_{abs}/ T_{con}(°C)	COP (-)	$\dot{Q}_{cool}$ (kW)	η_{ex} (%)
Parham et al. [56]	46.2	15	30/30	0.90	N.A. [1]	32.99
Al-Tahaineh [57]	90	5–10	N.A. [1]	0.75–0.81	10 kW	~35–36
Shehadi [59]	70–85	10	30	0.776	N.A. [1]	N.A. [1]
Kilic & Kaynakli [36]	80–95	5–10	30–40	0.75–0.80	N.A. [1]	25–35
Kumar et al. [58].	95	7	25/40	0.947	N.A. [1]	21.80
Saoud et al. [31].	82	4.5	35	0.749	11.03	62.2
Zaho et al. [60]	~90	N.A. [1]	N.A. [1]	0.795	N.A. [1]	N.A. [1]
Tawalbeh et al. [61].	~80–100	N.A. [1]	N.A. [1]	~0.70	~16	N.A. [1]
This study	78	6.5	30	0.797	20.68	36.93

[1] Not Available.

In addition to thermodynamic optimization, the overall feasibility of a solar-driven absorption cooling system is strongly influenced by the solar collector area and its associated cost. Increasing the collector surface improves the available driving heat and enhances the cooling capacity; however, it also raises installation and maintenance costs, potentially lowering the system's economic attractiveness. A sensitivity analysis conducted on the collector area indicates that beyond a certain threshold, the gain in performance (COP and cooling capacity) becomes marginal relative to the cost increase. Therefore, identifying an optimal balance between thermal performance and collector investment is essential for the practical deployment of solar absorption chillers. Future work will include detailed thermo-economic optimization to assess payback periods and system cost-effectiveness.

8. Conclusions, Limitations, and Recommendations

A clean energy-based, solar-powered absorption cooling system is being developed to enhance energy efficiency and environmental sustainability. The system leverages evacuated flat plate collectors to supply thermal energy to a stratified tank, which then drives a water–LiBr absorption chiller for cooling in small-to-medium-sized buildings. A multi-objective optimization framework based on Response Surface Methodology (RSM) was used to estimate the system's optimal performance. The input parameters—namely, the inlet temperatures of the heat exchangers, including those of the generator (T_{gen}), evaporator (T_{eva}), absorber (T_{abs}), and condenser (T_{con}) were defined according to the RSM design structure. The objective functions selected for optimization included the coefficient of performance (COP), cooling capacity ($\dot{Q}_{cool}$), and exergy efficiency (η_{ex}). The experimental design was structured using the Box–Behnken method. The key findings of this work can be summarized as follows:

- ANOVA analysis yielded regression models with good prediction accuracy for COP, $\dot{Q}_{cool}$, and η_{ex} Diagnostic plots, including predicted vs. actual and normal probability charts, confirmed the models' accuracy and statistical reliability.
- T_{abs} and T_{con} were identified as the most influential parameters across all responses. T_{eva} also showed a consistent and significant effect, while T_{gen} had a notable impact on $\dot{Q}_{cool}$ and COP, but it was not statistically significant for η_{ex}.
- For COP evaluation, the interactions $T_{abs} - T_{con}$ and $T_{gen} - T_{con}$ have significant *p*-values but low F-values, indicating limited relevance. Nonetheless, a low absorber

and condenser temperature, combined with a high generator temperature, results in an optimal COP of 0.8065.

- Through single-objective optimization, the system is configured for maximum at low condensing and absorbing temperatures, and high generator and evaporator temperatures, yielding 20.72 kW under the conditions: T_{gen} = 82 °C, T_{eva} = 4.5 °C, T_{abs} = 30 °C, and T_{con} = 30 °C.
- The single-objective optimization for exergy efficiency identifies the optimal conditions at: T_{gen} = 82 °C, T_{eva} = 2.5 °C, T_{abs} = 30 °C, and T_{con} = 35 °C, yielding an exergy efficiency of 39.29%.
- In the multi-objective optimization, the RSM optimizer predicts optimal values of COP = 0.7969, $\dot{Q}_{cool}$ = 20.68 kW, and η_{ex} = 36.93%, corresponding to T_{gen} = 78 °C, T_{eva} = 6.5 °C, T_{abs} = 30 °C, and T_{con} = 30 °C.
- The composite desirability is relatively high (=0.953), indicating that the selected settings yield favorable outcomes across all responses.

These findings provide a foundation for the implementation of a solar-powered water–LiBr absorption chiller, offering valuable insights into optimizing energy and exergy performance under real-world conditions. This contributes to improving the efficiency and sustainability of solar cooling systems. However, the study is limited to steady-state energy and exergy analyses, excluding transient behavior and dynamic operating scenarios. Additionally, optimization focuses on a limited set of input variables, without considering broader aspects like system cost and environmental impact. Future research should expand to include dynamic performance, along with integrated economic and environmental evaluations, for a more comprehensive system assessment. The proposed model is based on several simplifying assumptions. Steady-state operation was assumed, neglecting transient effects and short-term fluctuations in system behavior. Heat losses in pipes and auxiliary components were considered negligible, and solar input was treated as constant, ignoring daily and seasonal variations in irradiance. In addition, uncertainties related to thermophysical property correlations and numerical convergence may slightly affect the predicted values. While these assumptions are typical in thermodynamic simulations, they may introduce minor deviations from experimental data. Future work will address these limitations by incorporating transient analysis, detailed thermal losses, and refined property models to further improve prediction accuracy. The essential next step is to correlate the model's predictions with experimental data from a dedicated pilot system. This will serve to calibrate the model, quantify its real-world performance, and identify any areas requiring refinement.

Author Contributions: Conceptualization, A.S. and J.C.B.; methodology, A.S. and J.C.B.; software, A.S.; validation, A.S.; formal analysis, A.S.; investigation, A.S. and J.C.B.; data curation, A.S. and J.C.B.; writing—original draft preparation, A.S.; writing—review and editing, A.S. and J.C.B.; visualization, A.S.; supervision, J.C.B. All authors have read and agreed to the published version of the manuscript.

Funding: This research received no external funding.

Institutional Review Board Statement: Not applicable.

Informed Consent Statement: Not applicable.

Data Availability Statement: The data presented in this study are available on request from the corresponding author.

Conflicts of Interest: The authors declare no conflicts of interest.

Nomenclature

A_{Coll}	Collecting Area, m^2
$b_0 b_0$, b_i, b_{ii}, b_{ij}	Regression coefficients for the interception, linear, quadratic, and interaction terms
$\dot{C}_p$	Specific heat capacity, $kJ \cdot kg^{-1} \cdot K^{-1}$
$\dot{m_{coll}}$	Solar collector mass flow rate, $kg \cdot s^{-1}$
M_{st}	Mass of water in storage tank, kg
$\dot{Q}_{sol}$	Solar energy input, kW
$\dot{Q}_u$	Heat input to the ST, kW
$\dot{E}x_{Ph}$	Physical exergy
G_{tot}	Solar irradiation, $W \cdot m^{-2}$
$\dot{Q}$	thermal heat rate, kW
R^2	Coefficient of regression
R^2_{adj}	Adjusted coefficient of regression
R^2_{prd}	Predicted Coefficient of regression
$T_{c,i}$	Inlet temperature of the cold side, °C
$T_{h,i}$	Inlet temperature of the hot side, °C
$T_{c,i}$	Outlet temperature of the hot side, °C
$T_{h,o}$	Outlet temperature of the cold side, °C
U_{st}	Heat transfer coefficient, $W \cdot m^{-2} \cdot K^{-1}$
L_{st}	Tank Length, m
V_{st}	Tank Volume, m^3
X_i, X_j	Independent input parameter
Y_i	Predicted value of the response
h	Specific fluid enthalpy, $kJ \cdot kg^{-1}$
Ncoll	Number of collectors
P	Pressure, kPa
s	Specific entropy, $kJ \cdot kg^{-1}$
T	Temperature, °C
Tamb	Ambient Temperature, °C
Tf,moy	Mean temperature of the working fluid, °C
Tsun	Sun Temperature, K
UA	Area product, $kW \cdot °C^{-1}$
X	Lithium Bromide concentration, -
X_0	Center point Value
X_i	Actual (uncoded) value
x_i	Coded value of the i-th variable
X_i, X_j	Independent variables
Greek Symbol	
η_0	Optical efficiency (zero-order coefficient) of the collector, –
β_0	Offset term
$\in$	Statical error
$\dot{E}$	Exergy
ΔX	Step change corresponding to one coded unit of the *i*-th variable
ε	SHX Effectiveness, %
η	Efficiency, %
ρ	Density, kg/m^3
n	Number of factors
β	Regression coefficient
Abbreviations	
abs	Absorber
AC	Absorption chiller

amb	Ambient
ANOVA	Analysis of Variance
BBD	Box–Behnken Design
C.V.	Coefficient of variation
con	Condenser
Cool	Cooling output
COP	Coefficient of performance
COR	Coefficient of regression
Df	Degree of freedom
DoE	Design of Experiments
EES	Engineering Equation Solver
EFPC	Evacuated Flat Plate Collector
eva	Evaporator
ex	Exergy
f	Fluid
gen	Generator
H_2O-LiBr	Water–Lithium bromide
HTF	Heat Transfer Fluid
in	Inlet, input
is	Isentropic
LMTD	Log mean temperature difference, °C
out, e	Outlet, output
ref	Refrigerant (H_2O)
REV	Refrigerant Expansion Valve
RSM	Response Surface Methodology
SCR	Solution Circulation Ratio
SEV	Solution Expansion Valve
SHEX	Solution Heat Exchanger
sol	Solar
SP	Solution Pump
st	Storage tank
str	Strong solution (LiBr)
Subscripts and Superscripts	
tot	Total
wf	Working fluid
ws	Weak solution
dst	Destruction
th	Thermal

References

1. Jaiswal, K.K.; Chowdhury, C.R.; Yadav, D.; Verma, R.; Dutta, S.; Jaiswal, K.S.; Sangmesh, B.; Karuppasamy, K.S.K. Renewable and Sustainable Clean Energy Development and Impact on Social, Economic, and Environmental Health. *Energy Nexus* **2022**, *7*, 100118. [CrossRef]
2. Saoud, A.; Bouckchana, Y.; Fellah, A. Design of Solar-Driven Combined Heat and Power System: Parametric Study and Optimization. In Proceedings of the 2025 15th International Renewable Energy Congress (IREC), Hammamet, Tunisia, 2–4 February 2025. [CrossRef]
3. Maka, A.O.M.; Alabid, J.M. Solar Energy Technology and Its Roles in Sustainable Development. *Clean Energy* **2022**, *6*, 476–483. [CrossRef]
4. Saoud, A.; Boukhchana, Y.; Fellah, A. Performance Investigation and Working Fluid Evaluation for Organic Rankine Cycle Power Plant. In *Advances in Science, Technology & Innovation*; Springer: Cham, Switzerland, 2024; pp. 189–192. [CrossRef]
5. Qiu, Y.; He, Y.L.; Li, P.; Du, B.C. A Comprehensive Model for Analysis of Real-Time Optical Performance of a Solar Power Tower with a Multi-Tube Cavity Receiver. *Appl. Energy* **2017**, *185*, 589–603. [CrossRef]

6. González-Torres, M.; Pérez-Lombard, L.; Coronel, J.F.; Maestre, I.R.; Yan, D. A Review on Buildings Energy Information: Trends, End-Uses, Fuels and Drivers. *Energy Rep.* **2022**, *8*, 626–637. [CrossRef]
7. US Department of Energy. An Assessment of Energy Technologies and Research Opportunities. (Increasing Efficiency of Building Systems and Technologies). *Quadrenn. Technol. Rev.* **2015**, *38*, 12–19.
8. Bataineh, K.; Taamneh, Y. Review and Recent Improvements of Solar Sorption Cooling Systems. *Energy Build.* **2016**, *128*, 22–37. [CrossRef]
9. Lahoud, C.; El Brouche, M.; Lahoud, C.; Hmadi, M. A Review of Single-Effect Solar Absorption Chillers and Its Perspective on Lebanese Case. *Energy Rep.* **2021**, *7*, 12–22. [CrossRef]
10. Alshammari, N.K. Metaheuristic Energy Efficiency Optimization of Solar-Powered Absorption Cooling Systems under Operating Climactic Conditions Integrated with Explainable AI. *Case Stud. Therm. Eng.* **2025**, *69*, 106016. [CrossRef]
11. Lazrak, A.; Boudehenn, F.; Bonnot, S.; Fraisse, G.; Leconte, A.; Papillon, P.; Souyri, B. Development of a Dynamic Artificial Neural Network Model of an Absorption Chiller and Its Experimental Validation. *Renew. Energy* **2016**, *86*, 1009–1022. [CrossRef]
12. Kim, J.H.; Seong, N.C.; Choi, W. Forecasting the Energy Consumption of an Actual Air Handling Unit and Absorption Chiller Using Ann Models. *Energies* **2020**, *13*, 4361. [CrossRef]
13. Yang, S.; Wang, Y.; Wang, Y. Optimization of Cascade Cooling System Based on Lithium Bromide Refrigeration in the Polysilicon Industry. *Processes* **2021**, *9*, 1681. [CrossRef]
14. Bellos, E.; Tzivanidis, C. Optimum Design of a Solar Ejector Refrigeration System for Various Operating Scenarios. *Energy Convers. Manag.* **2017**, *154*, 11–24. [CrossRef]
15. Saoud, A.; Bruno, J.C.; Boukhchanaa, Y.; Fellah, A. Performance Investigation and Numerical Evaluation of a Single-Effect Double-Lift Absorption Chiller. *Appl. Therm. Eng.* **2023**, *227*, 120369. [CrossRef]
16. Domínguez-Inzunza, L.A.; Hernández-Magallanes, J.A.; Sandoval-Reyes, M.; Rivera, W. Comparison of the Performance of Single-Effect, Half-Effect, Double-Effect in Series and Inverse and Triple-Effect Absorption Cooling Systems Operating with the NH3–LiNO3 Mixture. *Appl. Therm. Eng.* **2014**, *66*, 612–620. [CrossRef]
17. Macriss, R.A.; Gutraj, J.M.; Zawacki, T.S. *Absorption Fluids Data Survey: Final Report on Worldwide Data*; Oak Ridge National Lab.: Oak Ridge, TN, USA, 1988.
18. Kaushik, S.C.; Kumar, R. Thermodynamic Study of a Two-Stage Vapour Absorption Refrigeration System Using NH3 Refrigerant with Liquid/Solid Absorbents. *Energy Convers. Manag.* **1985**, *25*, 427–431. [CrossRef]
19. Wang, M.; Infante Ferreira, C.A. Absorption Heat Pump Cycles with NH3–Ionic Liquid Working Pairs. *Appl. Energy* **2017**, *204*, 819–830. [CrossRef]
20. Hanel, A.; Seibold, T.; Gebhard, J.; Fendt, S.; Spliethoff, H. Evaluation of Influential Factors on Energy System Optimisation. *Energy Convers. Manag.* **2024**, *322*, 119156. [CrossRef]
21. Delbeke, J.; Runge-Metzger, A.; Slingenberg, Y.; Werksman, J. The Paris Agreement. In *Towards a Climate-Neutral Europe*; Routledge: London, UK, 2019; pp. 24–45. [CrossRef]
22. EES: Engineering Equation Solver | F-Chart Software: Engineering Software. Available online: https://fchartsoftware.com/ees/ (accessed on 28 December 2024).
23. Avanessian, T.; Ameri, M. Energy, Exergy, and Economic Analysis of Single and Double Effect LiBr–H_2O Absorption Chillers. *Energy Build.* **2014**, *73*, 26–36. [CrossRef]
24. Saoud, A.; Boukhchana, Y.; Bruno, J.C.; Fellah, A. Thermodynamic Investigation of an Innovative Solar-Driven Trigeneration Plant Based on an Integrated ORC-Single Effect-Double Lift Absorption Chiller. *Therm. Sci. Eng. Prog.* **2024**, *50*, 102596. [CrossRef]
25. Mohammadi, A.; Kasaeian, A.; Pourfayaz, F.; Ahmadi, M.H. Thermodynamic Analysis of a Combined Gas Turbine, ORC Cycle and Absorption Refrigeration for a CCHP System. *Appl. Therm. Eng.* **2017**, *111*, 397–406. [CrossRef]
26. Bellos, E.; Tzivanidis, C.; Antonopoulos, K.A. Exergetic, Energetic and Financial Evaluation of a Solar Driven Absorption Cooling System with Various Collector Types. *Appl. Therm. Eng.* **2016**, *102*, 749–759. [CrossRef]
27. Duffie, J.A.; Beckman, W.A. *Solar Engineering of Thermal Processes*, 4th ed.; John Wiley & Sons: Hoboken, NJ, USA, 2013. [CrossRef]
28. Bellos, E.; Tzivanidis, C. Parametric Analysis and Optimization of a Solar Driven Trigeneration System Based on ORC and Absorption Heat Pump. *J. Clean. Prod.* **2017**, *161*, 493–509. [CrossRef]
29. Bellos, E.; Tzivanidis, C.; Antonopoulos, K.A. Exergetic and Energetic Comparison of LiCl-H_2O and LiBr-H_2O Working Pairs in a Solar Absorption Cooling System. *Energy Convers. Manag.* **2016**, *123*, 453–461. [CrossRef]
30. Saoud, A.; Boukhchana, Y.; Fellah, A. Energetic Analysis and Assessment of a Single-Effect LiBr–H_2O Absorption Refrigeration System. In *Advances in Science, Technology & Innovation*; Springer: Cham, Switzerland, 2024; pp. 139–142. [CrossRef]
31. Saoud, A.; Boukhchana, Y.; Fellah, A. Thermal and Parametric Investigation of Solar-Powered Single-Effect Absorption Cooling System. *J. Therm. Anal. Calorim.* **2024**, *149*, 7469–7484. [CrossRef]
32. Pátek, J.; Klomfar, J. A Computationally Effective Formulation of the Thermodynamic Properties of LiBr–H_2O Solutions from 273 to 500 K over Full Composition Range. *Int. J. Refrig.* **2006**, *29*, 566–578. [CrossRef]

33. Pátek, J.; Klomfar, J. A Simple Formulation for Thermodynamic Properties of Steam from 273 to 523 K, Explicit in Temperature and Pressure. *Int. J. Refrig.* **2009**, *32*, 1123–1125. [CrossRef]
34. Akbari Kordlar, M.; Mahmoudi, S.M.S. Exergeoconomic Analysis and Optimization of a Novel Cogeneration System Producing Power and Refrigeration. *Energy Convers. Manag.* **2017**, *134*, 208–220. [CrossRef]
35. Petela, R. Exergy of Undiluted Thermal Radiation. *Sol. Energy* **2003**, *74*, 469–488. [CrossRef]
36. Kilic, M.; Kaynakli, O. Second Law-Based Thermodynamic Analysis of Water-Lithium Bromide Absorption Refrigeration System. *Energy* **2007**, *32*, 1505–1512. [CrossRef]
37. Bellos, E.; Tzivanidis, C.; Pavlovic, S.; Stefanovic, V. Thermodynamic Investigation of LiCl-H_2O Working Pair in a Double Effect Absorption Chiller Driven by Parabolic Trough Collectors. *Therm. Sci. Eng. Prog.* **2017**, *3*, 75–87. [CrossRef]
38. Mendoza, B. Total Solar Irradiance and Climate. *Adv. Space Res.* **2005**, *35*, 882–890. [CrossRef]
39. Borge, D.; Colmenar, A.; Castro, M.; Martín, S.; Sancristobal, E. Exergy Efficiency Analysis in Buildings Climatized with LiCl–H_2O Solar Cooling Systems That Use Swimming Pools as Heat Sinks. *Energy Build.* **2011**, *43*, 3161–3172. [CrossRef]
40. Kerme, E.D.; Chafidz, A.; Agboola, O.P.; Orfi, J.; Fakeeha, A.H.; Al-Fatesh, A.S. Energetic and Exergetic Analysis of Solar-Powered Lithium Bromide-Water Absorption Cooling System. *J. Clean. Prod.* **2017**, *151*, 60–73. [CrossRef]
41. Veza, I.; Spraggon, M.; Fattah, I.M.R.; Idris, M. Response Surface Methodology (RSM) for Optimizing Engine Performance and Emissions Fueled with Biofuel: Review of RSM for Sustainability Energy Transition. *Results Eng.* **2023**, *18*, 101213. [CrossRef]
42. Susaimanickam, A.; Manickam, P.; Joseph, A.A. A Comprehensive Review on RSM-Coupled Optimization Techniques and Its Applications. *Arch. Comput. Methods Eng.* **2023**, *30*, 4831–4853. [CrossRef]
43. Design-Expert | Stat-Ease. Available online: https://www.statease.com/software/design-expert/ (accessed on 25 January 2025).
44. Wang, J.; Wan, W. Experimental Design Methods for Fermentative Hydrogen Production: A Review. *Int. J. Hydrogen Energy* **2009**, *34*, 235–244. [CrossRef]
45. Chanioti, S.; Tzia, C. Optimization of Ultrasound-Assisted Extraction of Oil from Olive Pomace Using Response Surface Technology: Oil Recovery, Unsaponifiable Matter, Total Phenol Content and Antioxidant Activity. *LWT-Food Sci. Technol.* **2017**, *79*, 178–189. [CrossRef]
46. Yadav, A.M.; Chaurasia, R.C.; Suresh, N.; Gajbhiye, P. Application of Artificial Neural Networks and Response Surface Methodology Approaches for the Prediction of Oil Agglomeration Process. *Fuel* **2018**, *220*, 826–836. [CrossRef]
47. Kaushik, S.C.; Arora, A. Energy and Exergy Analysis of Single Effect and Series Flow Double Effect Water–Lithium Bromide Absorption Refrigeration Systems. *Int. J. Refrig.* **2009**, *32*, 1247–1258. [CrossRef]
48. Florides, G.A.; Kalogirou, S.A.; Tassou, S.A.; Wrobel, L.C. Design and Construction of a LiBr–Water Absorption Machine. *Energy Convers. Manag.* **2003**, *44*, 2483–2508. [CrossRef]
49. Ahmadi, S.; Khormali, A.; Meerovich Khoutoriansky, F. Optimization of the Demulsification of Water-in-Heavy Crude Oil Emulsions Using Response Surface Methodology. *Fuel* **2022**, *323*, 124270. [CrossRef]
50. Emeji, I.C.; Patel, B. Box-Behnken Assisted RSM and ANN Modelling for Biodiesel Production over Titanium Supported Zinc-Oxide Catalyst. *Energy* **2024**, *308*, 132765. [CrossRef]
51. Verma, A.; Ojha, K. Application of Response Surface Methodology for the Optimization of Viscosity of Foam Fracturing Fluids for the Unconventional Reservoir. *J. Nat. Gas Sci. Eng.* **2021**, *94*, 104086. [CrossRef]
52. Abdul Wahab, M.S.; Abd Rahman, S.; Abu Samah, R. Flux Model Development and Synthesis Optimization for an Enhanced GO Embedded Nanocomposite Membrane through FFD and RSM Approach. *Heliyon* **2020**, *6*, e05610. [CrossRef] [PubMed]
53. Jalilibal, Z.; Amiri, A.; Castagliola, P.; Khoo, M.B.C. Monitoring the Coefficient of Variation: A Literature Review. *Comput. Ind. Eng.* **2021**, *161*, 107600. [CrossRef]
54. Srivastava, M.; Maheshwari, S.; Kundra, T.; Rathee, S. Multi-Response Optimization of Fused Deposition Modelling Process Parameters of ABS Using Response Surface Methodology (RSM)-Based Desirability Analysis. *Mater. Today Proc.* **2017**, *4*, 1972–1977. [CrossRef]
55. Yang, P.; Chen, H.; Liu, Y.W. Application of Response Surface Methodology and Desirability Approach to Investigate and Optimize the Jet Pump in a Thermoacoustic Stirling Heat Engine. *Appl. Therm. Eng.* **2017**, *127*, 1005–1014. [CrossRef]
56. Parham, K.; Atikol, U.; Yari, M.; Agboola, O.P. Evaluation and Optimization of Single Stage Absorption Chiller Using (LiCl + H_2O) as the Working Pair. *Adv. Mech. Eng.* **2013**, *5*, 683157. [CrossRef]
57. Al-Tahaineh, H.A. Exergetic-Energetic Effectiveness of a Simple H_2O-LiBr Absorption Chiller Operated by Solar Energy Collected Using a Direct Flow Evacuated Tube Collector. *Int. J. Low-Carbon Technol.* **2023**, *18*, 689–696. [CrossRef]
58. Kumar, A.; Modi, A. Energy and Exergy Analysis of a Novel Ejector-Assisted Compression–Absorption–Resorption Refrigeration System. *Energy* **2023**, *263*, 125760. [CrossRef]
59. Shehadi, M. Optimizing Solar Cooling Systems. *Case Stud. Therm. Eng.* **2020**, *21*, 100663. [CrossRef]

60. Zhao, H.; Xu, H.; Jin, D.; An, W. Research on Geothermal-Driven Single-Effect Absorption Refrigeration Systems with Different Working Fluids: Energy and Exergy Analysis. *Int. J. Low-Carbon Technol.* **2024**, *19*, 1689–1698. [CrossRef]
61. Tawalbeh, M.; Salameh, T.; Albawab, M.; Al-Othman, A.; Assad, M.E.H.; Alami, A.H. Parametric Study of a Single Effect Lithium Bromide-Water Absorption Chiller Powered by a Renewable Heat Source. *J. Sustain. Dev. Energy Water Environ. Syst.* **2020**, *8*, 464–475. [CrossRef]